

RESEARCH ARTICLE | APRIL 10 2024

## Epitaxial growth of $\alpha\text{-(AlGa}_{1-x}\text{)}_2\text{O}_3$ by suboxide molecular-beam epitaxy at 1 $\mu\text{m/h}$

Jacob Steele  ; Kathy Azizie ; Naomi Pieczulewski ; Yunjo Kim ; Shin Mou ; Thaddeus J. Asel ; Adam T. Neal ; Debdeep Jena ; Huili G. Xing ; David A. Muller ; Takeyoshi Onuma ; Darrell G. Schlom 



*APL Mater.* 12, 041113 (2024)  
<https://doi.org/10.1063/5.0170095>



**APL Machine Learning**  
2023 Papers with Best Practices in Data Sharing and Comprehensive Background  
[Read Now](#)



# Epitaxial growth of $\alpha$ -(Al<sub>x</sub>Ga<sub>1-x</sub>)<sub>2</sub>O<sub>3</sub> by suboxide molecular-beam epitaxy at 1 $\mu$ m/h

Cite as: APL Mater. 12, 041113 (2024); doi: 10.1063/5.0170095

Submitted: 31 July 2023 • Accepted: 1 December 2023 •

Published Online: 10 April 2024



View Online



Export Citation



CrossMark

Jacob Steele,<sup>1,a)</sup> Kathy Azizie,<sup>1</sup> Naomi Pieczulewski,<sup>1</sup> Yunjo Kim,<sup>2</sup> Shin Mou,<sup>2</sup> Thaddeus J. Asel,<sup>2</sup> Adam T. Neal,<sup>2</sup> Debdeep Jena,<sup>1,3,4</sup> Huili G. Xing,<sup>1,3,4</sup> David A. Muller,<sup>3,5</sup> Takeyoshi Onuma,<sup>6</sup> and Darrell C. Schlom<sup>1,3,7</sup>

## AFFILIATIONS

<sup>1</sup>Department of Materials Science and Engineering, Cornell University, Ithaca, New York 14853, USA

<sup>2</sup>Air Force Research Lab, Materials and Manufacturing Directorate, Wright Patterson AFB, Dayton, Ohio 45433, USA

<sup>3</sup>Kavli Institute at Cornell for Nanoscale Science, Ithaca, New York 14853, USA

<sup>4</sup>Department of Electrical and Computer Engineering, Cornell University, Ithaca, New York 14853, USA

<sup>5</sup>School of Applied and Engineering Physics, Cornell University, Ithaca, New York 14853, USA

<sup>6</sup>Department of Applied Physics, Kogakuin University, 2665-1 Hachioji, Tokyo 192-0015, Japan

<sup>7</sup>Leibniz-Institut für Kristallzüchtung, Max-Born-Str. 2, 12489 Berlin, Germany

<sup>a)</sup>Author to whom correspondence should be addressed: [js3625@cornell.edu](mailto:js3625@cornell.edu)

## ABSTRACT

We report the use of suboxide molecular-beam epitaxy (S-MBE) to grow  $\alpha$ -(Al<sub>x</sub>Ga<sub>1-x</sub>)<sub>2</sub>O<sub>3</sub> films on (110) sapphire substrates over the  $0 < x < 0.95$  range of aluminum content. In S-MBE, 99.98% of the gallium-containing molecular beam arrives at the substrate in a preoxidized form as gallium suboxide (Ga<sub>2</sub>O). This bypasses the rate-limiting step of conventional MBE for the growth of gallium oxide (Ga<sub>2</sub>O<sub>3</sub>) from a gallium molecular beam and allows us to grow fully epitaxial  $\alpha$ -(Al<sub>x</sub>Ga<sub>1-x</sub>)<sub>2</sub>O<sub>3</sub> films at growth rates exceeding 1  $\mu$ m/h and relatively low substrate temperature ( $T_{\text{sub}} = 605 \pm 15$  °C). The ability to grow  $\alpha$ -(Al<sub>x</sub>Ga<sub>1-x</sub>)<sub>2</sub>O<sub>3</sub> over the nominally full composition range is confirmed by Vegard's law applied to the x-ray diffraction data and by optical bandgap measurements with ultraviolet-visible spectroscopy. We show that S-MBE allows straightforward composition control and bandgap selection for  $\alpha$ -(Al<sub>x</sub>Ga<sub>1-x</sub>)<sub>2</sub>O<sub>3</sub> films as the aluminum incorporation  $x$  in the film is linear with the relative flux ratio of aluminum to Ga<sub>2</sub>O. The films are characterized by atomic-force microscopy, x-ray diffraction, and scanning transmission electron microscopy (STEM). These  $\alpha$ -(Al<sub>x</sub>Ga<sub>1-x</sub>)<sub>2</sub>O<sub>3</sub> films grown by S-MBE at record growth rates exhibit a rocking curve full width at half maximum of  $\approx 12$  arc secs, rms roughness  $< 1$  nm, and are fully commensurate for  $x \geq 0.5$  for 20–50 nm thick films. STEM imaging of the  $x = 0.78$  sample reveals high structural quality and uniform composition. Despite the high structural quality of the films, our attempts at doping with silicon result in highly insulating films.

© 2024 Author(s). All article content, except where otherwise noted, is licensed under a Creative Commons Attribution (CC BY) license (<https://creativecommons.org/licenses/by/4.0/>). <https://doi.org/10.1063/5.0170095>

## I. INTRODUCTION

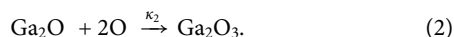
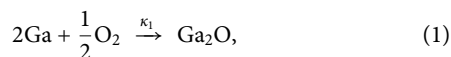
There are four polymorphs of Ga<sub>2</sub>O<sub>3</sub> that are commonly studied in the literature: trigonal ( $\alpha$ ), monoclinic ( $\beta$ ), cubic ( $\gamma$ ), and orthorhombic ( $\kappa$ ).<sup>1–3</sup> Of these, the monoclinic  $\beta$ -Ga<sub>2</sub>O<sub>3</sub> is the most researched as it is the most thermodynamically stable polymorph under standard conditions and has readily available bulk-grown substrates.<sup>1,4</sup>  $\beta$ -Ga<sub>2</sub>O<sub>3</sub> is a promising semiconductor material with

an ultrawide bandgap of 4.6–4.9 eV, a large theoretical breakdown field of 8 MV/cm, controllable n-type doping, high electron mobility, and optical transparency.<sup>3,5–9</sup> These properties give  $\beta$ -Ga<sub>2</sub>O<sub>3</sub> a Baliga figure of merit for vertical power devices operating at a low frequency that exceeds those of the current commercial semiconductors for power electronics, i.e., silicon, SiC, and GaN, for applications in high power devices with increased power density and performance.<sup>3,9,10</sup>

Even with Ga<sub>2</sub>O<sub>3</sub>'s ultrawide bandgap, one thrust of Ga<sub>2</sub>O<sub>3</sub> research has been extending its properties further through alloying with Al<sub>2</sub>O<sub>3</sub>.<sup>11</sup> These (Al<sub>x</sub>Ga<sub>1-x</sub>)<sub>2</sub>O<sub>3</sub> semiconductor alloys are attractive for a range of tunable bandgaps from 4.6 to 8.6 eV.<sup>12</sup> The differences in the crystal structure and lattice constant in going from pure Ga<sub>2</sub>O<sub>3</sub> ( $x = 0$ ) to pure Al<sub>2</sub>O<sub>3</sub> ( $x = 1$ ) have resulted in two approaches for alloying. One approach is to stick to the monoclinic  $\beta$ -(Al<sub>x</sub>Ga<sub>1-x</sub>)<sub>2</sub>O<sub>3</sub> polymorph, which is the stable phase for pure Ga<sub>2</sub>O<sub>3</sub>. The range of  $x$  that has been achieved in this  $\beta$ -(Al<sub>x</sub>Ga<sub>1-x</sub>)<sub>2</sub>O<sub>3</sub> approach to date is  $0 \leq x \leq 0.61$ , leading to a bandgap range of 4.6–5.9 eV.<sup>13</sup> An alternative option is the  $\alpha$ -(Al<sub>x</sub>Ga<sub>1-x</sub>)<sub>2</sub>O<sub>3</sub> approach, which is the stable phase for pure Al<sub>2</sub>O<sub>3</sub>. This approach has the advantage that alloying over the entire range of  $x$  in  $\alpha$ -(Al<sub>x</sub>Ga<sub>1-x</sub>)<sub>2</sub>O<sub>3</sub> has been experimentally achieved.<sup>12,13</sup> This has extended the obtainable bandgaps of  $\alpha$ -(Al<sub>x</sub>Ga<sub>1-x</sub>)<sub>2</sub>O<sub>3</sub> to the full range of 5.4–8.6 eV, surpassing both AlN (6.0 eV) and diamond (5.5 eV).<sup>12,14</sup>

There are multiple epitaxial growth methods available for the growth of  $\alpha$ -(Al<sub>x</sub>Ga<sub>1-x</sub>)<sub>2</sub>O<sub>3</sub> thin films. Thus far, molecular-beam epitaxy (MBE) has demonstrated the highest quality growths over the full range of  $x$  of all growth methods.<sup>12</sup> MBE is a technique for the growth of high-quality thin films in an ultra-high vacuum environment using high-purity molecular beams, which are typically produced by thermal evaporation from heated crucibles containing molten liquid or solid source materials, which are conventionally elemental.<sup>15–21</sup> MBE allows a high level of control over growth conditions with the trade-off of relatively slow growth rates when it comes to the growth of  $\alpha$ -(Al<sub>x</sub>Ga<sub>1-x</sub>)<sub>2</sub>O<sub>3</sub>. For example, it has been shown that MBE growth of  $\beta$ -(Al<sub>x</sub>Ga<sub>1-x</sub>)<sub>2</sub>O<sub>3</sub> can stabilize films up to  $x = 0.61$  at growth rates up to 0.04  $\mu\text{m}/\text{h}$ ,<sup>13</sup> while non-MBE methods have been limited to a maximum  $x = 0.52$ .<sup>22,23</sup> Nevertheless, for  $\alpha$ -(Al<sub>x</sub>Ga<sub>1-x</sub>)<sub>2</sub>O<sub>3</sub>, MBE<sup>12,24,25</sup> and other growth techniques, including pulsed laser deposition (PLD),<sup>26</sup> metal-organic chemical vapor deposition (MOCVD),<sup>26</sup> magnetron sputtering,<sup>27</sup> mist chemical vapor deposition (CVD),<sup>28</sup> and hydride vapor phase epitaxy (HVPE),<sup>29,30</sup> have been able to grow thin films over the full composition range. For conventional MBE, the maximum growth rate achieved for  $\alpha$ -(Al<sub>x</sub>Ga<sub>1-x</sub>)<sub>2</sub>O<sub>3</sub> in the literature has been 0.12  $\mu\text{m}/\text{h}$ .<sup>25</sup>

In conventional MBE, elemental sources are heated to create molecular fluxes that react with supplied ozone or oxygen plasma to oxidize the supplied metal and create the desired film. For Ga<sub>2</sub>O<sub>3</sub>, this process involves the two-step reaction seen in the following equations:<sup>31–33</sup>



The first reaction step, Eq. (1), involves the formation of a suboxide, Ga<sub>2</sub>O, which is then further oxidized in the second reaction step, Eq. (2), to form Ga<sub>2</sub>O<sub>3</sub>. For many oxides of metals with 3+ valence, including Ga<sub>2</sub>O<sub>3</sub>, the intermediary suboxide is highly volatile compared to both the metal and metal oxide. For Ga<sub>2</sub>O<sub>3</sub>, the first reaction step is rate limiting because the volatility of Ga<sub>2</sub>O leads to a short surface residence lifetime that limits the amount of Ga<sub>2</sub>O that can oxidize and incorporate before desorption, removing oxygen adatoms from the surface. This problem is further exacerbated by the competition that Ga<sub>2</sub>O has with elemental gallium for

oxygen adatoms in the conventional reaction. As a result, the two-step growth kinetics of conventional MBE growth of Ga<sub>2</sub>O<sub>3</sub>, in combination with the high volatility of Ga<sub>2</sub>O, results in typical maximum growth rates of around 0.1  $\mu\text{m}/\text{h}$ .<sup>12,24,34</sup> Additionally, the Ga<sub>2</sub>O<sub>3</sub> formed can react with gallium adatoms to form Ga<sub>2</sub>O and reduce the growth rate, resulting in a decrease in the growth rate of Ga<sub>2</sub>O<sub>3</sub> as the gallium flux increases past the stoichiometric ratio.<sup>31,32</sup> The available growth mechanisms prevent adsorption control for the conventional MBE growth of Ga<sub>2</sub>O<sub>3</sub>. This is a challenge as the growth of thin films of oxides of metals with 3+ valence in the adsorption-controlled regime has been associated with improved crystal quality, suppression of undesired oxidation states, and reduced formation of compensating defects.<sup>35–42</sup>

To circumvent the kinetic limitations of conventional MBE, an alternative MBE technique called suboxide MBE (S-MBE) has been employed. S-MBE involves supplying suboxide molecular beams, here Ga<sub>2</sub>O, rather than elemental, i.e., gallium, molecular beams. This allows the rate-limiting first reaction step, Eq. (1), of conventional MBE to be skipped and removes the competition between gallium and Ga<sub>2</sub>O.<sup>43</sup> As a result, the single-step reaction kinetics in Eq. (2) for S-MBE are simpler, and the growth window under which the formation of high-quality Ga<sub>2</sub>O<sub>3</sub> films is possible is significantly expanded. Additionally, the removal of elemental gallium prevents the etching of Ga<sub>2</sub>O<sub>3</sub> to form Ga<sub>2</sub>O, enabling adsorption-controlled growth. Adsorption control occurs when the surface is flooded with excess Ga<sub>2</sub>O such that all of the oxygen adatoms are used up and the surplus Ga<sub>2</sub>O desorbs. This results in a constant growth rate for all higher Ga<sub>2</sub>O fluxes beyond the stoichiometric ratio; the growth rate in the adsorption-controlled regime is controlled only by the ozone flux. With these simplified growth kinetics, S-MBE can be utilized to grow epitaxial thin films of Ga<sub>2</sub>O<sub>3</sub> at growth rates over an order of magnitude higher than conventional MBE growth rates at relatively low growth temperatures and with high film quality.<sup>43,44</sup> In this work, we apply S-MBE to the growth of  $\alpha$ -(Al<sub>x</sub>Ga<sub>1-x</sub>)<sub>2</sub>O<sub>3</sub> and find that thin films with unparalleled structural perfection can be grown over the full range of  $x$  at rates exceeding 1  $\mu\text{m}/\text{h}$ .

## II. METHODS

For the growth of  $\alpha$ -(Al<sub>x</sub>Ga<sub>1-x</sub>)<sub>2</sub>O<sub>3</sub> films by S-MBE, we use an elemental aluminum (6N purity) source and a Ga<sub>2</sub>O suboxide source formed by mixing liquid gallium metal (Alfa Aesar, 7N purity) and solid Ga<sub>2</sub>O<sub>3</sub> powder (Alfa Aesar, 5N purity). The purity of the Ga<sub>2</sub>O<sub>3</sub> powder is the highest commercially available but is still relatively low for an MBE source and may be a source of contamination that limits device-quality growths. The gallium + Ga<sub>2</sub>O<sub>3</sub> mix has a  $\approx 0.4$  molecular fraction of oxygen that is calculated to provide a 99.98% Ga<sub>2</sub>O molecular beam.<sup>43</sup> The gallium + Ga<sub>2</sub>O<sub>3</sub> mixture is contained within a BeO (Materion, 99.7% purity) crucible, and the aluminum is contained within a pyrolytic boron nitride crucible. The low purity of the BeO crucible is also a concern, but the Ga<sub>2</sub>O<sub>3</sub> + gallium mix allows growth fluxes at much lower temperatures than that for a pure Ga<sub>2</sub>O<sub>3</sub> source, significantly reducing the contamination from the crucible and Ga<sub>2</sub>O<sub>3</sub> powder.<sup>43</sup> Both the crucibles are loaded into retractable dual-filament, medium-temperature MBE effusion cells. Retractable effusion cells allow much more efficient implementation of the S-MBE method for Ga<sub>2</sub>O<sub>3</sub> as the Ga<sub>2</sub>O<sub>3</sub> + gallium mix needs to be changed to prevent demixing and degradation after

three to four days of growth. The effusion cells are mounted to a Veeco Gen10 MBE system and outgassed to the desired growth temperature to remove impurities immediately before growth.

The flux of the molecular and atomic beams is measured *in situ* with a quartz crystal microbalance (QCM). The  $10 \times 10 \text{ mm}^2$   $\text{Al}_2\text{O}_3$  substrates are back-side coated with a 10 nm thick titanium adhesion layer, followed by 200 nm of platinum to enable radiative thermal heating, and  $T_{\text{sub}}$  is measured with an optical pyrometer operating at a wavelength of 980 nm. All substrates are held in substrate holders made of Haynes<sup>®</sup> 214<sup>®</sup> alloy for low outgassing and high oxidation resistance.

An elemental aluminum source is used rather than an aluminum suboxide source due to source instabilities encountered in our previous attempts at  $\text{Al}_2\text{O}$  sources.<sup>45</sup> Unfortunately, elemental aluminum sources have a tendency to climb over the crucible walls when a tip filament is heated and a tendency to clog (by oxidation of the surface) if a tip filament is not heated.<sup>45</sup> We only heat the base filament to prevent source damage and use a retractable source so that the source can be changed if the source begins to clog.<sup>45</sup> Further motivation for an elemental aluminum source comes from Ellingham diagrams, showing aluminum to reduce  $\text{Ga}_2\text{O}$  as well as be oxidized by the ozone to form an  $\text{Al}_2\text{O}$  flux.<sup>46</sup>

The A-plane  $\text{Al}_2\text{O}_3$  substrates were cleaned with isopropanol, acetone, Micro-90<sup>®</sup>, and water and then annealed in open air at  $1000^\circ\text{C}$  for 10 h. The growth on these A-plane  $\text{Al}_2\text{O}_3$  substrates was performed in  $\sim 80\%$  distilled ozone under a background pressure of  $P_{\text{O}_3} = 5 \times 10^{-6}$  Torr, while varying the substrate temperature,  $T_{\text{sub}}$ , from  $590$  to  $880^\circ\text{C}$ . The  $\text{Ga}_2\text{O}$  flux was fixed at  $(1.55 \pm 0.4) \times 10^{15}$  molecules  $\text{cm}^{-2} \text{ s}^{-1}$ , and the aluminum flux varied from  $0$  to  $4.6 \times 10^{15}$  atoms  $\text{cm}^{-2} \text{ s}^{-1}$  to control the value of  $x$  over the  $0 < x < 0.95$  range as described in the next section.

Vacuum ultraviolet-visible transmittance was used to measure the optical bandgaps of a set of  $\alpha\text{-(Al}_x\text{Ga}_{1-x})_2\text{O}_3$  films to confirm the aluminum content of the  $\alpha\text{-(Al}_x\text{Ga}_{1-x})_2\text{O}_3$  films. For these measurements, the transmittance spectra were in the UVC spectral range at room temperature (RT). On each film, the Ti/Pt back-side metal coating was removed by mechanical polishing, and the backside of the sapphire substrate was additionally polished using a chemical-mechanical polishing process to obtain a mirror surface. The spectra were measured at RT using monochromatic light in the wavelength range of  $140\text{--}300$  nm from a deuterium lamp dispersed by a 20 cm focal-length Czerny–Turner monochromator (Bunkoukeiki KV-200) equipped with a 2400 groove/mm grating. The spectral resolution at 160 nm was set as 0.2 eV (4 nm) with a slit width of 2 mm. The transmitted light was detected using a photomultiplier tube through a window coated with sodium salicylate.

Scanning transmission electron microscopy (STEM) was conducted on selected samples to further assess the film microstructure quality. The samples were prepared using a Thermo Fisher Helios G4 UX Focused Ion Beam with a final milling step of 5 keV. The STEM measurements were taken with an aberration-corrected Thermo Fisher Spectra 300 CFEG operated at 300 keV. High-angle annular dark-field (HAADF) imaging and energy dispersive x-ray spectroscopy (EDS) were used to investigate the structural quality and confirm composition uniformity, respectively.

All the reciprocal space maps (RSM), rocking curves, and x-ray reflectivity (XRR) measurements were performed at room

temperature with a PANalytical Empyrean XRD system equipped to provide  $\text{Cu K}\alpha_1$  radiation. The rocking curves were measured in a triple-axis configuration using a 220 germanium analyzer crystal for the film and substrate 110 peaks of each sample. Asymmetric RSMs were measured on each film to determine whether the film was commensurately strained to or relaxed from the substrate. A multimeter was used for a two-point measurement of each film's resistance at room temperature. The surfaces of the films were investigated by atomic force microscopy (AFM) using an Asylum Research Cypher Environmental AFM.

### III. RESULTS AND DISCUSSION

Using S-MBE to grow  $\alpha\text{-(Al}_x\text{Ga}_{1-x})_2\text{O}_3$ , we first determined what range of compositions,  $x$ , can be grown, whether the resulting films are high quality, and what growth rates are obtainable, while maintaining high film quality. The initial experiments explored a wide range of growth conditions on A (110), C (001), and M (100) plane sapphire substrates to determine which orientation produces the highest quality  $\alpha\text{-(Al}_x\text{Ga}_{1-x})_2\text{O}_3$  films. C-plane sapphire has been utilized for  $\alpha\text{-(Al}_x\text{Ga}_{1-x})_2\text{O}_3$  growth over nearly the entire range of  $x$ <sup>47</sup> but can nucleate a transition to  $(201)\beta\text{-(Al}_x\text{Ga}_{1-x})_2\text{O}_3$ .<sup>48</sup> It is also observed on other orientations that C-plane facets form and nucleate the transition to  $\beta\text{-(Al}_x\text{Ga}_{1-x})_2\text{O}_3$ .<sup>12,48</sup> For this reason, A-plane and M-plane substrates are promising as they are perpendicular to the C-plane and may prevent C-plane faceting from nucleating the transition to  $\beta\text{-(Al}_x\text{Ga}_{1-x})_2\text{O}_3$  to achieve stability over the full range of  $x$ .<sup>12,24</sup> In the initial experiments, it was found that the A-plane substrates provided the largest growth window, highest growth rates, and the highest quality  $\alpha\text{-(Al}_x\text{Ga}_{1-x})_2\text{O}_3$  films. For these reasons, A-plane substrates were used for all of the films discussed in this paper.

At  $T_{\text{sub}} = 590^\circ\text{C}$  and a gallium suboxide flux  $\Gamma_{\text{Ga}_2\text{O}} = 1.5 \times 10^{15}$  molecules  $\text{cm}^{-2} \text{ s}^{-1}$ , the initial  $\alpha\text{-Ga}_2\text{O}_3$  thin film was grown at  $1.2 \mu\text{m/h}$ . With these high growth rates, each film was grown for one minute to achieve a film thickness of  $20\text{--}48$  nm. These growth parameters were used as the default growth conditions, while the aluminum flux,  $\Gamma_{\text{Al}}$ , was varied between each growth to change the aluminum incorporation  $x$ . It is seen that the aluminum adatoms are kinetically limiting, possibly due to their two-step reaction, increasing the competition with  $\text{Ga}_2\text{O}$  for oxygen adatoms and leading to  $\text{Ga}_2\text{O}$  desorption as the film quality rapidly decreased above  $x = 0.2$  at  $T_{\text{sub}} = 590^\circ\text{C}$ . This was remedied simply by increasing  $T_{\text{sub}}$  by  $10^\circ\text{C}$ . The temperature was increased by  $10^\circ\text{C}$  two more times over the set of growths as  $\Gamma_{\text{Al}}$  increased from  $0$  atoms  $\text{cm}^{-2} \text{ s}^{-1}$  to the maximum  $4.6 \times 10^{15}$   $\text{cm}^{-2} \text{ s}^{-1}$ . This resulted in a range of growth temperatures of  $T_{\text{sub}} = 605 \pm 15^\circ\text{C}$ . In this range, we were able to achieve high-quality thin film growth for compositions of  $0 < x < 0.95$ . Interestingly, growing homoepitaxial  $\text{Al}_2\text{O}_3$  ( $x = 1$ ) results in poly-crystalline, rough films up to the maximum achievable  $T_{\text{sub}}$  of  $880^\circ\text{C}$  in our MBE system, regardless of whether  $\text{Ga}_2\text{O}$  is supplied or not. This is consistent with the reports in the literature of the growth temperatures used for homoepitaxial  $\text{Al}_2\text{O}_3$  films by MBE:  $800^\circ\text{C}$  for A-plane sapphire<sup>24</sup> and  $750^\circ\text{C}$  for homoepitaxy on M-plane sapphire.<sup>12</sup> With the  $(10\text{--}30)\times$  higher growth rate of our work compared to the prior studies, the need for higher substrate temperatures for adatom mobility and reactivity is not surprising. Our result points to the benefit that an emerging technique called

thermal laser epitaxy has for the growth of  $\text{Al}_2\text{O}_3$  and other materials that are challenging for MBE.<sup>49</sup> We also note that as the  $\text{Ga}_2\text{O}$  source's mix separates and degrades over time,  $\Gamma_{\text{Ga}}$  unintentionally drifts in the range of  $(1.55 \pm 0.4) \times 10^{15}$  molecules  $\text{cm}^{-2} \text{s}^{-1}$  over the set of growths. Due to the high growth rates and inhomogeneous flux distribution on the substrate, the films should be rotated to provide at least one full rotation for each monolayer grown to average out the flux inhomogeneity and prevent compositional oscillations in the film, as shown in Fig. S2 of the supplementary material. If

desired, such a composition gradient could be used to create chiral layers with precise thickness control by the ratio of the growth rate and rotation speed.<sup>50</sup>

We show in Fig. 1 that S-MBE can be utilized to grow  $\alpha\text{-(Al}_x\text{Ga}_{1-x})_2\text{O}_3$  over the  $0 < x < 0.95$  composition range. This is seen by the 110 peak shifting from the  $2\theta$  position of  $\alpha\text{-Ga}_2\text{O}_3$  ( $x = 0$ ) to nearly that of  $\alpha\text{-Al}_2\text{O}_3$  ( $x = 1$ ) shown in Fig. 1(b). In Fig. 1, each of the film peaks has growth fringes, or Laue oscillations, which are associated with high structural quality in thin epitaxial films.<sup>51</sup> Additionally, Fig. 1(a) shows that the  $\alpha\text{-(Al}_x\text{Ga}_{1-x})_2\text{O}_3$  films are single phase as there are no additional peaks over the range of  $2\theta$  from  $15^\circ$  to  $60^\circ$ . Each competing phase has peaks that appear in this range of  $2\theta$ . The individual XRD plots for all films are shown in Figs. S3(a)–S15(a) of the supplementary material. From the  $2\theta$  position, each  $x$  value is determined using Vegard's law.<sup>52</sup> Vegard's law assumes that the lattice parameter varies linearly with alloy composition, which has been confirmed for  $\alpha\text{-(Al}_x\text{Ga}_{1-x})_2\text{O}_3$  in the literature.<sup>53</sup> This method only works well when there is a well-defined film peak separated from the substrate peak, which we observe in each film up to  $x = 0.88$ . Above this aluminum fraction, the film peak begins to overlap with the substrate peak so the

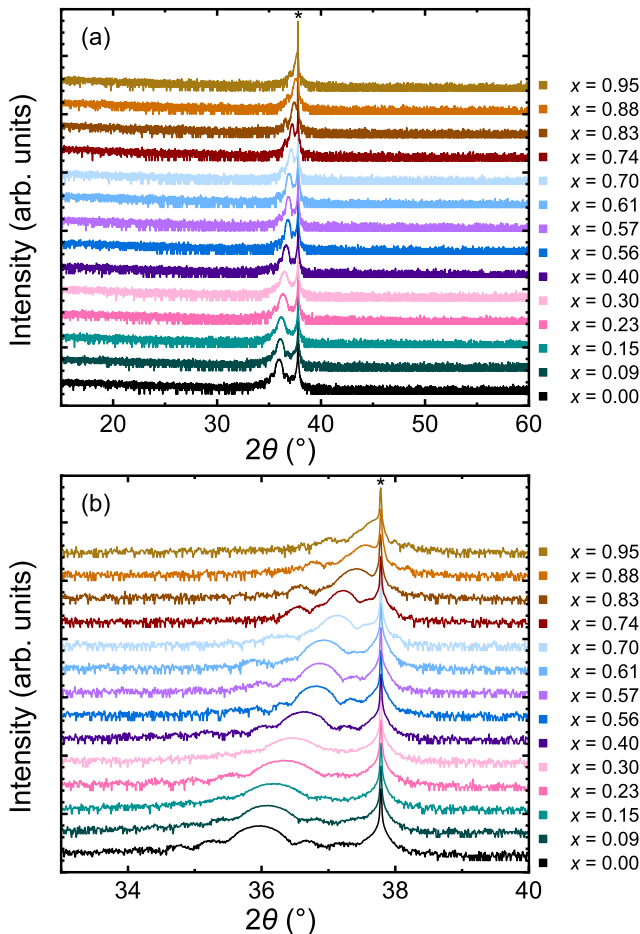


**FIG. 1.** (a)  $\theta$ - $2\theta$  XRD scans of all of the samples presented in Table I over the  $2\theta$  range of  $15^\circ$ – $60^\circ$ , and offset for clarity along the logarithmic vertical axis. The plots show that the films are single phase with no additional peaks observed. The composition of each film is given by the color of the individual plot. The 110 peak of the  $\alpha\text{-Al}_2\text{O}_3$  substrate is marked by an asterisk (\*). (b) A zoomed-in view of the  $\theta$ - $2\theta$  XRD scans shown in (a) over the range of  $2\theta = 33^\circ$ – $40^\circ$ . The  $\alpha\text{-(Al}_x\text{Ga}_{1-x})_2\text{O}_3$  peaks shift monotonically over the entire range from  $2\theta = 35.94^\circ$ , corresponding to  $\alpha\text{-Ga}_2\text{O}_3$  ( $x = 0$ ), to just below  $2\theta = 37.8^\circ$ , corresponding to  $\alpha\text{-Al}_2\text{O}_3$  ( $x = 1$ ). The large peak at  $2\theta = 37.8^\circ$  for each film is due to the 110 peak of the sapphire substrate and is marked by an asterisk (\*). Each film shows Laue fringes around the film peak. The composition of each film is determined from its 110 peak position, except the  $x = 0.95$  film, for which the 220 peak position was used in combination with Vegard's law. All the films shown have growth rates exceeding  $1 \mu\text{m/h}$ . The exact growth rates for each film are presented in Table I.

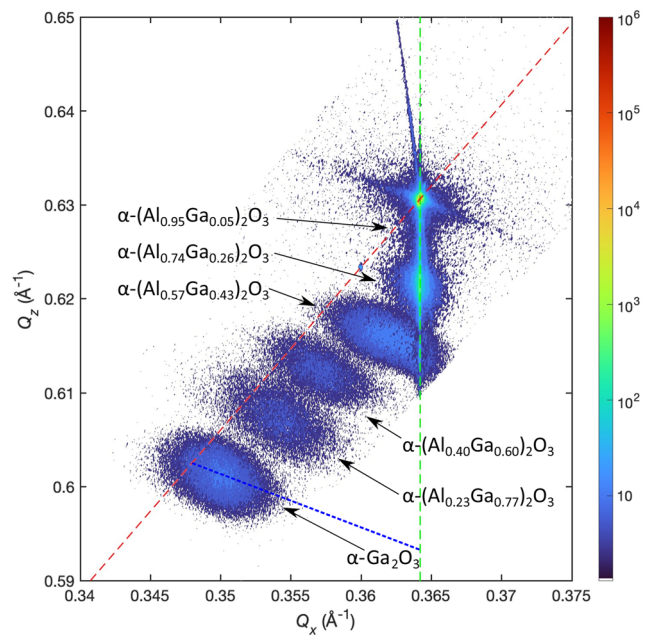


**FIG. 2.** Superimposed asymmetric RSMs at the 300 peak for a subset of the samples presented in Table I across the entire range of  $x$ . In this figure, the intensity is measured in counts per second. The  $x$  and  $y$  axes are positions in reciprocal space that are calculated by  $Q_x = \frac{4\pi}{\lambda} \sin(\frac{2\theta}{2} - \omega) \times \sin(\frac{2\theta}{2})$  and  $Q_z = \frac{4\pi}{\lambda} \cos(\frac{2\theta}{2} - \omega) \times \sin(\frac{2\theta}{2})$ . In this equation,  $Q_x$  and  $Q_y$  are the reciprocal lattice spacings,  $\lambda$  is the wavelength of Cu  $K\alpha_1$  radiation, and both  $2\theta$  and  $\omega$  correspond to the normal XRD terminology. The dashed green line corresponds to where the films are fully strained, and the dashed red line shows where films are fully relaxed. The dashed blue line is the relaxation line along which the lattice parameters change for  $\alpha\text{-Ga}_2\text{O}_3$ . The lower  $x$  films are nearly completely relaxed, and the high  $x$  films are completely strained to the substrate. The transition point from relaxed to strained for these thicknesses is around  $x = 0.57$ , which shows a mixed strained–relaxed structure.

18 April 2024 00:37:15

220 peak was used to maintain adequate separation between the film and substrate peaks in  $2\theta$  and give a well-defined peak position to apply Vegard's law. Another complication is that Vegard's law assumes that the films are relaxed and deviates for films that are strained to the substrate. The films in our study are a mix of relaxed and strained, as shown in Fig. 2. In our experiments the strained films are compressively strained to the substrate, resulting in an extension of the out-of-plane lattice parameter. This leads to a reduction in the  $2\theta$  position and an underestimation of  $x$  in the strained films. This effect is more significant for commensurately strained films of lower  $x$  as they contain larger strains. For example,  $\alpha\text{-(Al}_{0.57}\text{Ga}_{0.43}\text{)}_2\text{O}_3$  is corrected from  $\alpha\text{-(Al}_{0.51}\text{Ga}_{0.49}\text{)}_2\text{O}_3$ ,  $\alpha\text{-(Al}_{0.83}\text{Ga}_{0.17}\text{)}_2\text{O}_3$  is corrected from  $\alpha\text{-(Al}_{0.80}\text{Ga}_{0.20}\text{)}_2\text{O}_3$ , and  $\alpha\text{-(Al}_{0.95}\text{Ga}_{0.05}\text{)}_2\text{O}_3$  has no substantial change. We also see that the "relaxed" films have a residual strain, but the strain is small, and the correction results in a difference in  $x$  of less than 0.01 for all the relaxed films shown.

To confirm the high structural quality suggested by the Laue oscillations, the rocking curves were measured. The  $x = 0.95$  film did not have a rocking curve taken since the film and substrate peaks overlap and prevent an accurate measurement. Overall, the rocking curves for the films showed an average full width at half maximum (FWHM) of 12 arc sec for the films and 11 arc sec for the substrates. There was a maximum difference of 4 arc sec between a film and substrate. These FWHM are comparable to the instrumental resolution of the XRD employed, revealing that both the film and substrate are of high structural quality. The individual rocking curve FWHMs for all films are presented in Table I. The individual rocking curve plots for all films are shown in Figs. S3(b)–S15(b) of the supplementary material.

To probe the surface quality, atomic force microscopy (AFM) was used on each sample over a  $5 \times 5 \mu\text{m}^2$  area. The results of these measurements are presented in Table I. The results show that

a typical film has an rms roughness of less than 1 nm and that the rms roughness increases as  $x$  decreases. This can be understood as a reduction in the surface quality as the lattice mismatch between  $\alpha\text{-(Al}_x\text{Ga}_{1-x}\text{)}_2\text{O}_3$  and  $\alpha\text{-Al}_2\text{O}_3$  increases with decreasing  $x$ . This effect dominates over the expected increase in surface roughness as the film thickness increases with  $x$  increasing from 0.00 (20 nm) to 0.95 (48 nm). The individual rms roughness values for all films are presented in Table I, and the individual AFM plots for all films are shown in Figs. S3(c)–S15(c) of the supplementary material.

Figure 3 shows these characterization techniques applied to an example film with a middling composition of  $\alpha\text{-(Al}_{0.40}\text{Ga}_{0.60}\text{)}_2\text{O}_3$ . Figure 3(a) again shows that the film displays Laue oscillations, suggesting high structural quality. In Figs. 3(c) and 3(d), the rocking curves reveal that the film has high structural quality. The film and substrate rocking curves have FWHM values of 16 and 15 arc sec, respectively. Finally, in Fig. 3(b), the AFM image of the 23.4 nm thick film exhibits an rms roughness of 0.77 nm. In the AFM, it is also seen that the surface structure is stepped, matching the surface structure of the substrate and confirming epitaxial growth kinetics. RHEED intensity oscillations were seen in the growth of this film confirming that epitaxy occurs via a layer-by-layer growth.<sup>54</sup>

In Table I, there are multiple trends between the growth conditions and film properties. First, there is a positive trend in the growth rate with the supplied aluminum flux,  $\Gamma_{\text{Al}}$ . The dependence is shown to be approximately linear in Fig. 4(a). This shows that the aluminum is readily incorporated into the films as  $\Gamma_{\text{Ga}_2\text{O}}$  is held nearly constant, and the difference in the growth rate is primarily contributed by aluminum. In Fig. S1 of the supplementary material, it is shown that in our tested growth conditions,  $\text{Al}_2\text{O}_3$  is much more stable than  $\text{Ga}_2\text{O}$ , with a vapor pressure a factor of  $10^{-5}$  times that of  $\text{Ga}_2\text{O}$ .<sup>46</sup> This suggests that substrate temperature may be used as a method to control the composition,  $x$ , by selectively desorbing  $\text{Ga}_2\text{O}$ . Nonetheless, in our measurements, each data point is given a

**TABLE I.** Growth conditions and structural characteristics of each film in the study. The  $\text{Ga}_2\text{O}$  flux for all films was in the range of  $(1.55 \pm 4) \times 10^{15}$  molecules  $\text{cm}^{-2} \text{s}^{-1}$ . An average of all of the films is also presented in Table II for comparison against other studies.

$x$ ...	$T_{\text{sub}}$ ( $^{\circ}\text{C}$ )	$\text{Ga}_2\text{O}$ flux $10^{14}$ ( $\text{cm}^{-2}\text{s}^{-1}$ )	$\text{Al}$ flux $10^{14}$ ( $\text{cm}^{-2}\text{s}^{-1}$ )	Growth rate ( $\mu\text{m}/\text{h}$ )	Film FWHM (arc sec)	Substrate FWHM (arc sec)	rms roughness (nm)	Film thickness (nm)
0.95	620	12.0	46	2.87	...	...	0.435	47.9
0.88	620	12.0	37	2.45	13	9	0.521	40.9
0.83	620	13.6	34	2.01	13	14	0.308	33.5
0.74	610	13.6	25	2.36	11	9	0.551	39.3
0.70	610	14.0	23	1.95	14	14	0.543	32.5
0.61	610	15.1	13	1.81	11	9	0.646	30.1
0.57	600	19.4	16	1.74	12	12	0.409	29
0.56	620	11.6	11	1.64	11	8	0.326	27.3
0.40	600	16.3	6.9	1.4	15	16	0.773	23.4
0.30	600	13.2	2.7	1.34	11	8	0.970	22.4
0.23	600	16.3	2.8	1.07	11	12	0.915	17.8
0.15	590	14.7	1.1	1.15	12	13	1.01	19.1
0.09	600	16.3	0.67	1.22	11	9	1.13	20.3
0.00	590	15.5	0	1.2	12	12	1.06	20.0
Average	605	$15.5 \pm 4$	...	...	12	11	0.67	

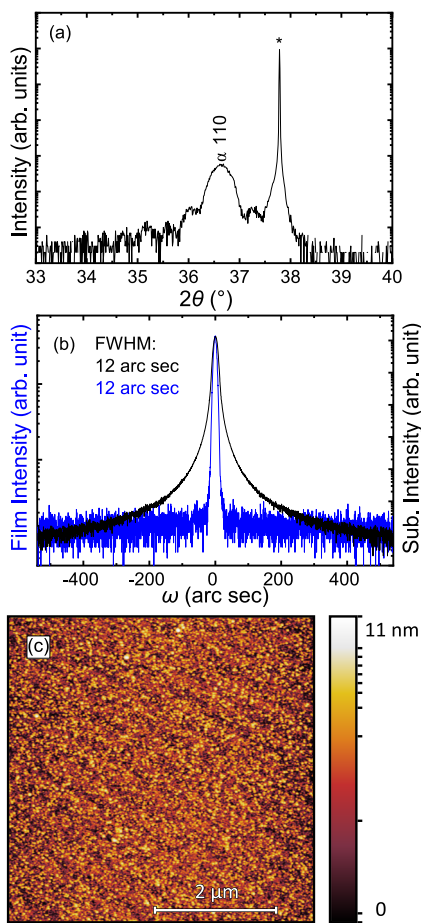
shape to mark the substrate temperature,  $T_{\text{sub}}$ , and the trend shows that the linear dependence is relatively temperature-independent. Additionally, we do not reach adsorption-controlled growth conditions even at the highest fluxes, which are significantly above the fluxes necessary for adsorption control during S-MBE of  $\beta\text{-Ga}_2\text{O}_3$ .<sup>44</sup>

Figure 4(b) shows the dependence of  $x$  on the aluminum flux fractions:  $\Gamma_{\text{Al}}/(\Gamma_{\text{Al}}+\Gamma_{\text{Ga}_2\text{O}})$  and  $\Gamma_{\text{Al}}/(\Gamma_{\text{Al}}+2\Gamma_{\text{Ga}_2\text{O}})$ , where  $2\Gamma_{\text{Ga}_2\text{O}}$  represents the number of gallium atoms supplied by each  $\text{Ga}_2\text{O}$  molecule. Our expectation was that at the experimental  $T_{\text{sub}}$ , aluminum should be fully incorporated, while  $\text{Ga}_2\text{O}$  is selectively desorbed, resulting in a significantly higher incorporation of aluminum than gallium, especially at higher  $T_{\text{sub}}$ . It is observed that  $x$  is linear with the aluminum flux fraction at  $T_{\text{sub}} = 605 \pm 15^\circ\text{C}$  and aluminum is preferentially incorporated. Similar to Fig. 4(a), each data point is given a shape to show that the linear behavior is not significantly dependent on

$T_{\text{sub}}$ . The linear behavior is unexpected and suggests that each  $\text{Ga}_2\text{O}$  adatom only contributes approximately one gallium atom to the film, rather than the two gallium atoms that are expected. This contribution of one gallium atom per  $\text{Ga}_2\text{O}$  supplied is consistent with what is observed in the studies on the S-MBE growth of  $\beta\text{-Ga}_2\text{O}_3$  films.<sup>44</sup> This may be explained by only a fraction of the  $\text{Ga}_2\text{O}$  flux sticking at the  $T_{\text{sub}}$ . Figure 4(b) also shows that the aluminum flux is preferentially incorporated into the films as the slope of  $\Gamma_{\text{Al}}/(\Gamma_{\text{Al}} + 2\Gamma_{\text{Ga}_2\text{O}})$  is significantly greater than unity. This can be explained by a reduction in the amount of  $\text{Ga}_2\text{O}$  incorporation with an increase in the aluminum flux, potentially due to aluminum increasingly reducing  $\text{Ga}_2\text{O}$  to gallium. Comparing the amount of gallium incorporated into the film using the thickness measured by XRR to the incident flux of gallium measured by the QCM, equal to  $2 \times \Gamma_{\text{Ga}_2\text{O}}$ , implies that approximately half of the gallium supplied is incorporated at  $x = 0$  and that the incorporated fraction drops as  $x$  increases. Despite the complications above, the linear behavior of the flux fraction  $\Gamma_{\text{Al}}/(\Gamma_{\text{Al}}+\Gamma_{\text{Ga}_2\text{O}})$  allows simple control of  $x$  by balancing the flux *in situ* with methods such as QCM.

It has been shown that  $\alpha\text{-(Al}_x\text{Ga}_{1-x})_2\text{O}_3$  films have a critical thickness, dependent on  $x$ , at which relaxation begins to occur.<sup>25</sup> Asymmetric reciprocal space maps (RSMs) were measured for each film at the 300 peak to determine whether the films are strained to or relaxed from the substrate. The results of these measurements are aggregated and shown in Fig. 2, with the red line representing the calculated film values in  $Q_x - Q_z$  space. The films are strained when their in-plane lattice parameter,  $Q_x^{-1}$ , matches that of the substrate, which is shown by the dashed green line in Fig. 2. For  $\alpha\text{-(Al}_x\text{Ga}_{1-x})_2\text{O}_3$  films in the 20–48 nm range, it is seen that the low  $x$  samples are nearly completely relaxed and only become slightly more strained with increasing  $x$  up to approximately  $x = 0.57$ . At  $x = 0.57$ , the film transitions to a mixed strained-relaxed character. At all  $x > 0.57$ , the films are fully compressively strained to the substrate. As the transition from strained to relaxed begins at a critical thickness, which varies with composition, we would expect to see the strain relaxation occur at a higher  $x$  with increasing film thickness. This finding matches that of a previous study, which suggests that as the lattice mismatch between  $\alpha\text{-(Al}_x\text{Ga}_{1-x})_2\text{O}_3$  and  $\alpha\text{-Al}_2\text{O}_3$  is reduced with increasing  $x$ , the films are more easily strained to the substrate.<sup>24</sup> This is corroborated by the trend of reduced surface roughness with increasing  $x$ , as presented in Table I, even with increasing film thickness.

As a confirmation of our compositional control and as a check of the XRD method used to extract  $x$ , we measured the optical bandgap for a set of  $\alpha\text{-(Al}_x\text{Ga}_{1-x})_2\text{O}_3$  films. The set of films ranges in composition from  $0.00 < x < 0.79$  and was grown specifically for the optical bandgap measurements. These films were grown with higher film thicknesses than those presented in Table I, ranging from 18 to 73 nm, and at high rotational speeds (20 rpm) to avoid any potential composition gradients. Figure 5(a) shows the transmittance spectra of these films. Each film was measured using wavelengths over the range of 140–300 nm, corresponding to photon energies of 8.86–4.13 eV. According to density functional theory calculations,  $\alpha\text{-(Al}_x\text{Ga}_{1-x})_2\text{O}_3$  has an indirect bandgap throughout the alloy composition range, with the difference between direct and indirect bandgaps increasing from 5 meV for  $x = 0$  to 270 meV for  $x = 1$ .<sup>42</sup> Nevertheless, the direct optical interband transitions allowed at the  $\Gamma$ -point are dominantly observed in the optical spectra.



**FIG. 3.** (a)  $\theta$ - $2\theta$  XRD scan of the  $\alpha\text{-(Al}_{0.40}\text{Ga}_{0.60})_2\text{O}_3$  film over the  $2\theta$  range of  $2\theta = 33^\circ$ – $40^\circ$ . Laue fringes are observed on both sides of the film peak. The asterisk (\*) marks the 110 peak of the substrate. (b) The XRD rocking curve of the film, shown in blue, shows a strong match to the substrate and exhibits a FWHM of 12 arc sec. The rocking curve of the substrate, shown in black, also has a FWHM of 12 arc sec. (c) AFM reveals that the growth surface of the same film is stepped, just like the underlying substrate. The surface exhibits an rms roughness of 0.77 nm; the film thickness is 23.4 nm.

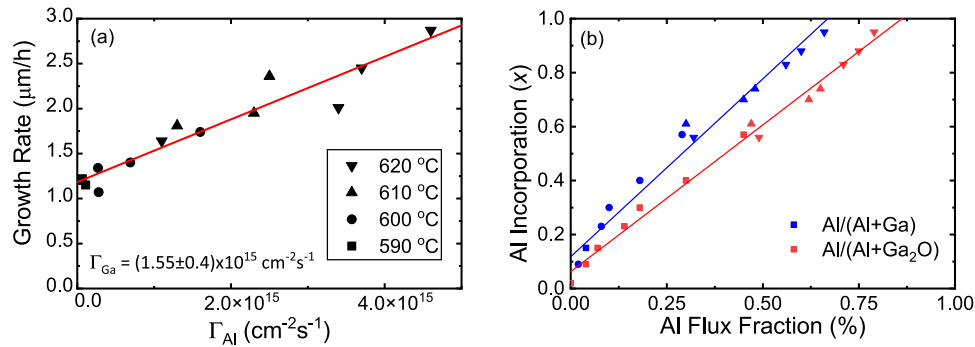


**FIG. 4.** (a) Plot of the film growth rate as a function of the aluminum flux,  $\Gamma_{\text{Al}}$ , from Table I for the set of growths with  $\Gamma_{\text{Ga}_2\text{O}} = (1.55 \pm 0.4) \times 10^{15} \text{ cm}^{-2} \text{ s}^{-1}$ . There is an approximately linear increase in the growth rate with  $\Gamma_{\text{Al}}$ . The different shapes of the data points correspond to the films grown at different  $T_{\text{sub}}$ , which are given by the legend in (a). This reveals that there is not a strong dependence of the growth rate on  $T_{\text{sub}}$ . (b) Plot of the dependence of  $x$  on the aluminum flux fraction ( $\Gamma_{\text{Al}}/\Gamma_{\text{Tot}}$ ) to determine how effectively each species is incorporating. The blue points correspond to the flux fraction of  $\Gamma_{\text{Al}}/(\Gamma_{\text{Al}} + \Gamma_{\text{Ga}_2\text{O}})$ . The red points correspond to the flux fraction of  $\Gamma_{\text{Al}}/(\Gamma_{\text{Al}} + 2 \times \Gamma_{\text{Ga}_2\text{O}})$ , where  $2 \times \Gamma_{\text{Ga}_2\text{O}}$  represents the amount of gallium supplied. It is seen that the dependence is approximately linear with no significant temperature dependence for both flux fractions. Note that the ratio of  $\Gamma_{\text{Al}}/(\Gamma_{\text{Al}} + 2 \times \Gamma_{\text{Ga}_2\text{O}})$  has a slope significantly above unity, which suggests that not all of the supplied gallium incorporates into the films. This is supported by the flux fraction of  $\Gamma_{\text{Al}}/(\Gamma_{\text{Al}} + \Gamma_{\text{Ga}_2\text{O}})$  being much closer to unity, suggesting that each  $\text{Ga}_2\text{O}$  molecule incident on the substrate only contributes approximately one gallium to the growing film.

**TABLE II.** Comparison of the average growth conditions and structural characteristics of the films in this study to other studies on the growth of  $\alpha\text{-(Al}_x\text{Ga}_{1-x})_2\text{O}_3$  by MBE. All other studies use PAMBE with M-plane sapphire and demonstrate growth over the nominally full range of  $x$ . We show that S-MBE achieves record growth rate, structural quality, and surface quality with favorable growth conditions of low  $T_{\text{sub}}$  and  $P_{\text{Ozone}}$ .

Study	Growth method	$\text{Al}_2\text{O}_3$ Substrate orientation	$T_{\text{sub}}$ °C	$P_{\text{Ozone}}$ or $P_{\text{plasma}}$ (Torr)	Max growth rate ( $\mu\text{m/h}$ )	Best FWHM (arc sec)	Best rms roughness (nm)
This study	S-MBE	A	$605 \pm 15$	$5 \times 10^{-6}$	2.90	12 avg	0.67 avg
Kumaran <i>et al.</i> <sup>24</sup>	PAMBE	A and M	800	$2 \times 10^{-5}$	0.12	...	...
Jinno <i>et al.</i> <sup>12</sup>	PAMBE	M	650–750	$1 \times 10^{-6} - 1 \times 10^{-5}$	0.04	1200	0.78
McCandless <i>et al.</i> <sup>25</sup>	PAMBE	M	625–680	...	...	900	0.99

Therefore,  $(ah\nu)^2$  is plotted as a function of the photon energy,  $h\nu$ , shown in Fig. 5(b) to extract the direct optical bandgap energies. The linear regression gives the energy of the direct absorption edge at the  $\Gamma$  point. Here, the indirect character is known to induce a large broadening of the absorption onset.<sup>12,53,55</sup> Furthermore, an excitonic effect is observed even at RT and may induce a shoulder or further broadening of the absorption onset.<sup>12,53,55</sup> The excitonic effect induces a shoulder near the absorption edge for  $x \leq 0.33$ . The shoulder and tail parts of the spectra are excluded to extract the direct optical bandgap energy by linear regression. Previous absorption and spectroscopic ellipsometry studies show the existence of a higher-energy transition at around 6.0–6.3 eV for  $\alpha\text{-Ga}_2\text{O}_3$ .<sup>55,56</sup> Contribution from the higher-energy transitions is excluded in the fitting analyses. The measured bandgap energies,  $E_g$ , are plotted as a function of  $x$ , as shown in Fig. 5(c). The bowing parameter,  $b$ , is estimated to be  $(1.0 \pm 0.2)$  eV, assuming a quadratic dependence of  $E_g$  on  $x$ , as shown by the solid line in Fig. 5(c). In the fitting,  $E_g$  of  $\alpha\text{-Al}_2\text{O}_3$  and  $\alpha\text{-Ga}_2\text{O}_3$  are taken as 8.6 and 5.4 eV, respectively.<sup>12</sup> The value of  $b$  exceeds that reported for C-plane  $\alpha\text{-(Al}_x\text{Ga}_{1-x})_2\text{O}_3$  films,<sup>53</sup> is slightly smaller than the 1.1 eV reported for M-plane

$\alpha\text{-(Al}_x\text{Ga}_{1-x})_2\text{O}_3$  films,<sup>12</sup> and is much lower than the 1.37 eV predicted by first-principles calculations.<sup>42</sup> From theory, the difference in  $b$  may be attributed to the large broadening of the absorption onset.

We contextualize our measurements by comparing the growth conditions and film properties to other studies involving the growth  $\alpha\text{-(Al}_x\text{Ga}_{1-x})_2\text{O}_3$  using MBE presented in Table II. These other studies differ in using plasma-assisted molecular-beam epitaxy (PAMBE) rather than S-MBE and tend to use M-plane sapphire substrates rather than A-plane. Each of these studies also stabilized  $\alpha\text{-(Al}_x\text{Ga}_{1-x})_2\text{O}_3$  over the nominally full range of  $x$ . Nonetheless, it is seen that S-MBE provides favorable growth conditions with a substantially lower  $T_{\text{sub}}$  and relatively low  $P_{\text{Ozone}}$ . At these growth conditions, we reach growth rates over  $2.5 \mu\text{m/h}$ , significantly higher than in conventional MBE. Generally, increased growth rates and lowered temperatures are associated with reductions in the film quality through reduced surface kinetics. Despite the  $20\times$  increase in the growth rate, our films also show record structural quality with a reduction of nearly  $100\times$  in the FWHM of the film rocking curves compared to previous  $\alpha\text{-(Al}_x\text{Ga}_{1-x})_2\text{O}_3$  films grown by conventional MBE. The surface quality is also competitive, with

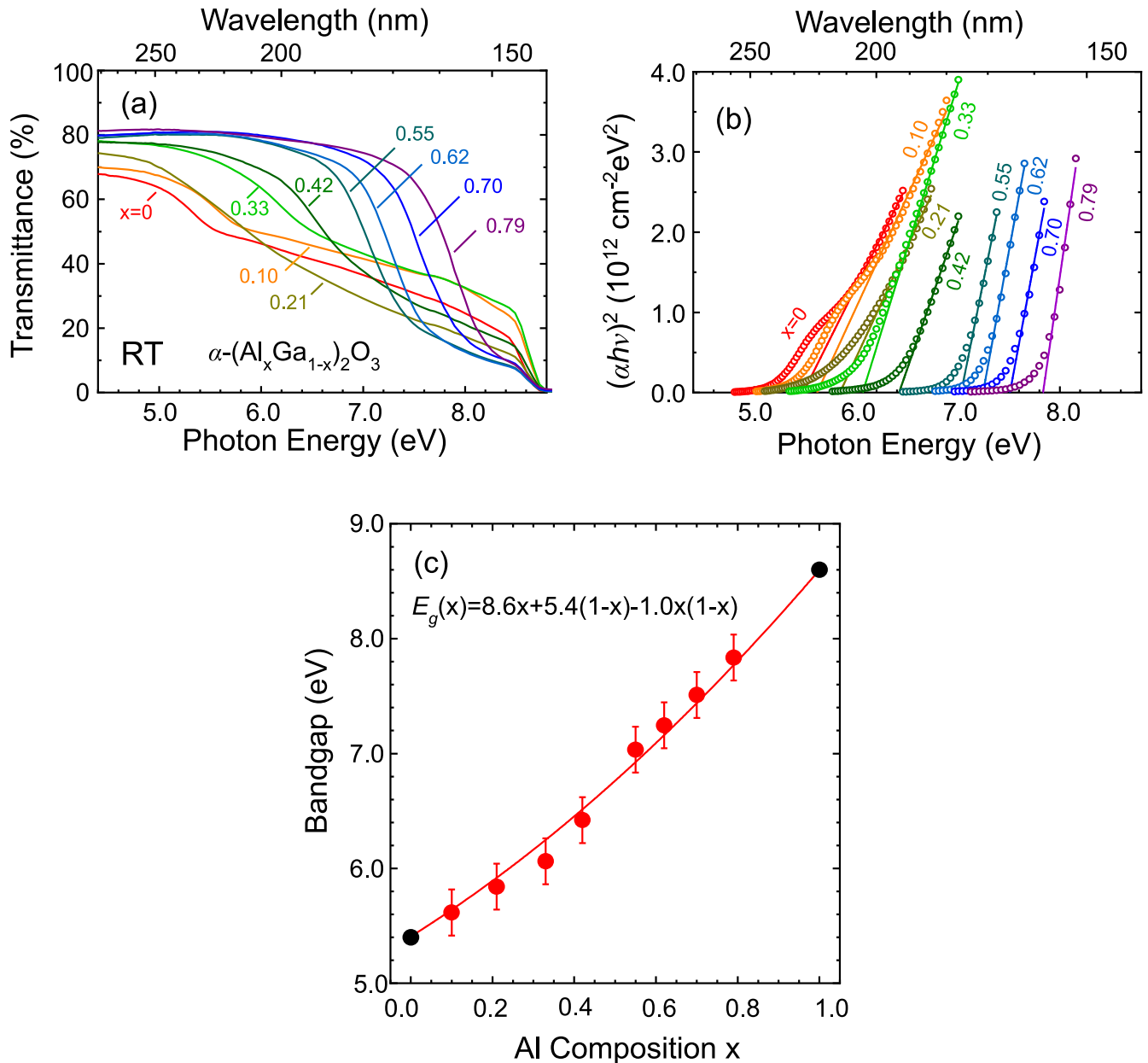


**FIG. 5.** (a) The transmittance spectra of a set of  $\alpha\text{-(Al}_x\text{Ga}_{1-x}\text{)}_2\text{O}_3$  films over the UVC spectral range of 140–300 nm at RT. These samples were grown for this measurement, and their corresponding XRD measurements are shown in Fig. S16 of the supplementary material. The absorption coefficient  $\alpha$  is calculated by  $\alpha = \ln\left(\frac{1-R}{T}\right)/d$ , where  $R$ ,  $T$ , and  $d$  represent the reflectance, transmittance, and film thickness, respectively. (b)  $(\alpha h\nu)^2$  is plotted as a function of the photon energy,  $h\nu$ . The shoulder and tail parts are excluded to extract the bandgap by linear regression. (c) A plot of the bandgap as a function of aluminum composition,  $x$ . Assuming a quadratic dependence of  $E_g$  on  $x$  to estimate the bowing parameter, we find  $b = (1.0 \pm 0.20)$  eV. The solid red line shows the fit of the bandgap as a function of  $x$ , accounting for  $b$ .

the average rms below 1 nm. The improved growth kinetics of S-MBE over conventional MBE growth methods are demonstrated by the favorable, low  $T_{\text{sub}}$  growth conditions with record MBE growth rates and film quality over nominally the entire range of  $x$ .

To further demonstrate the quality of the films, HAADF-STEM images of the  $\alpha\text{-(Al}_{0.78}\text{Ga}_{0.22}\text{)}_2\text{O}_3$  film are shown in Fig. 6. To avoid

layers of varying composition along the growth direction, the films shown in Figs. 5 and 6 were grown at 20 rpm. The film was grown at  $T_{\text{sub}} = 625^\circ\text{C}$  at  $1.50 \mu\text{m/h}$  for five minutes, totaling 125 nm in thickness. The film has an rms roughness of 0.89 nm measured by AFM, shown in Fig. S18(a) of the supplementary material, and a rocking curve FWHM of 15 arc sec for the film and 16 arc sec for the sub-

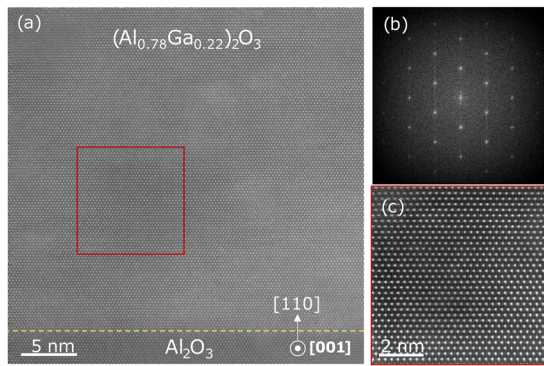


**FIG. 6.** (a) HAADF-STEM image of the  $\alpha$ - $(\text{Al}_{0.78}\text{Ga}_{0.22})_2\text{O}_3$  film grown on an A-plane sapphire substrate. The dashed yellow line indicates the interface between the  $\text{Al}_2\text{O}_3$  (110) substrate and the grown  $\alpha$ - $(\text{Al}_{0.78}\text{Ga}_{0.22})_2\text{O}_3$  film. (b) FFT of (a) showing a single set of sharp diffraction peaks. The FFT quantifies the lattice matching of  $\alpha$ - $(\text{Al}_{0.78}\text{Ga}_{0.22})_2\text{O}_3$  to the sapphire. (c) HAADF-STEM image of the enlarged region (red) in (a) showing single-phase  $\alpha$ - $(\text{Al}_{0.78}\text{Ga}_{0.22})_2\text{O}_3$  with no visible defects.

strate, shown in Fig. S18(b) of the supplementary material. This film also shows that *S*-MBE can grow films with record structural quality compared to previous MBE studies, as presented in Table II, while also being thicker than these previous studies. Figure 6(a) shows a clean interface between single phase epitaxial  $\alpha$ - $(\text{Al}_{0.78}\text{Ga}_{0.22})_2\text{O}_3$  and the substrate. The fast Fourier transform (FFT) in Fig. 6(b) across the interface shows that the epitaxial film is strained to the sapphire substrate. The higher resolution image in Fig. 6(c) highlights the high structural quality and lack of defects in the  $\alpha$ - $(\text{Al}_{0.78}\text{Ga}_{0.22})_2\text{O}_3$  film. In Fig. S17 of the supplementary material, energy dispersive x-ray spectroscopy (EDS) mapping shows that the aluminum and gallium fractions are also consistent throughout the bulk of the  $\alpha$ - $(\text{Al}_x\text{Ga}_{1-x})_2\text{O}_3$  epitaxial film.

Once high-quality growths were achieved over the nominally full composition range, we attempted to dope  $\alpha$ - $(\text{Al}_x\text{Ga}_{1-x})_2\text{O}_3$  with silicon. This was done using a  $\text{SiO}_2$  source that was flux calibrated using an Arrhenius fit of the thickness, which was measured using XRR.<sup>44</sup> The target doping concentration of silicon was  $1 \times 10^{19} \text{ cm}^{-3}$  for all growths. This concentration was selected to attempt to fill the existing traps without introducing Si-Si dimer traps in hopes of creating mobile carriers. Nine compositions of  $\alpha$ - $(\text{Al}_x\text{Ga}_{1-x})_2\text{O}_3$  from  $0 < x < 0.75$ , both commensurately strained and relaxed, were grown and measured. These films ranged in thickness from 12.1 to 38.1 nm. For all doping attempts, none of the films were conductive enough to get a two-point reading for the resistance on a multimeter, meaning that the resistance is, at least, in the  $\text{M}\Omega$  range. This high resistance prevented Hall measurements from determining the electron mobility and sheet carrier concentration. There was no change in the growth rate, composition, or film structural quality (as assessed by RHEED, XRD, and AFM) when the  $\text{SiO}_2$  source was used. The transition from relaxed to strained was around  $x = 0.5$  for films  $\leq 40$  nm thick and did not appear to impact the doping efficacy as both the relaxed and strained films overloaded the multimeter. It is unclear whether the silicon is not being successfully incorporated, the silicon is only partially incorporated, or if the silicon is incorporated

but not contributing mobile electrons. To help determine which of these occurs, we grew a 120 nm thick  $\alpha$ - $(\text{Al}_{0.71}\text{Ga}_{0.29})_2\text{O}_3$  film and a 125 nm thick  $\alpha$ - $(\text{Al}_{0.74}\text{Ga}_{0.26})_2\text{O}_3$  film for temperature-dependent Hall measurements. Both the films had  $5 \times 10^{19} \text{ cm}^{-3}$  Si doping targeted. The temperature-dependent Hall measurements showed that both the films were insulating up to 1000 K with a current of only 10 nA with 10 V applied at 1000 K.

#### IV. CONCLUSIONS

In this paper, we apply *S*-MBE, a variant of MBE with improved growth kinetics, to the growth of  $\alpha$ - $(\text{Al}_x\text{Ga}_{1-x})_2\text{O}_3$ . We show that *S*-MBE can be utilized to overcome the kinetic challenges involved in the conventional MBE growth of  $\alpha$ - $(\text{Al}_x\text{Ga}_{1-x})_2\text{O}_3$  and likely other oxides of metals with 3+ valence. This is demonstrated by the growth of high quality  $\alpha$ - $(\text{Al}_x\text{Ga}_{1-x})_2\text{O}_3$  under low  $T_{\text{sub}}$  growth conditions with growth rates exceeding  $1 \mu\text{m/h}$  on A-plane sapphire substrates. These kinetic improvements through *S*-MBE are promising for using  $\alpha$ - $(\text{Al}_x\text{Ga}_{1-x})_2\text{O}_3$  layers in device structures.

We hypothesized that the incident flux from the aluminum molecular beam would incorporate at a significantly higher rate than the incident flux from the  $\text{Ga}_2\text{O}$  molecular beam since the  $\text{Ga}_2\text{O}$  is much more volatile than  $\text{Al}_2\text{O}$ . It is indeed observed that aluminum preferentially incorporates in this temperature range. At the  $T_{\text{sub}}$  utilized in this study and with no aluminum present, only  $\sim 50\%$  of  $\text{Ga}_2\text{O}$  is found to incorporate as gallium in the final film. As the aluminum flux increases, the incorporation efficacy of  $\text{Ga}_2\text{O}$  is seen to reduce further, potentially due to aluminum reducing  $\text{Ga}_2\text{O}$ . Despite this, we observe that the growth rate is approximately linear with the combined aluminum +  $\text{Ga}_2\text{O}$  flux and that  $x$  is nearly linear with the aluminum flux fraction in the substrate temperature range of  $605 \pm 15^\circ\text{C}$ . The linear behavior can be beneficial for synthesizing  $\alpha$ - $(\text{Al}_x\text{Ga}_{1-x})_2\text{O}_3$  thin films as it allows simple control of the aluminum incorporation along the incorporation line.

Going forward, there are multiple directions for the  $\alpha$ - $(\text{Al}_x\text{Ga}_{1-x})_2\text{O}_3$  research. One of the most significant is achieving mobile carriers in  $\alpha$ - $(\text{Al}_x\text{Ga}_{1-x})_2\text{O}_3$ . We attempted doping the  $\alpha$ - $(\text{Al}_x\text{Ga}_{1-x})_2\text{O}_3$  films with various compositions and thicknesses with  $\sim 1 \times 10^{19} \text{ cm}^{-3}$  silicon. We found that all tested films are too resistive for Hall measurements regardless of composition or strain. It is unknown whether the resistivity is because silicon is not being incorporated successfully or whether the silicon is incorporated but not activated. Theoretical calculations predict that silicon donors will only be shallow up to  $x = 0.72$ , which would explain why the highest aluminum content films do not conduct.<sup>57</sup> Future work will look at post-annealing the Si-doped  $\alpha$ - $(\text{Al}_x\text{Ga}_{1-x})_2\text{O}_3$  films to see whether the carriers can be activated. Other dopants, such as germanium or tin, may also be tested in the future experiments at varying compositions and doping levels.

Another challenge is that all films shown in Fig. 1 and Table I have thicknesses below 50 nm. This can be useful for layers in modern devices, but there is also interest in growing thicker films for vertical device structures, especially to utilize the rapid growth rates of *S*-MBE. It is shown that the  $\alpha$ - $(\text{Al}_{0.78}\text{Ga}_{0.22})_2\text{O}_3$  film shown in Fig. 6 shows that *S*-MBE can grow films over 100 nm thick, while maintaining record structural quality. Additionally, growing films to  $\mu\text{m}$  thicknesses can improve doping by avoiding interface depletion. Growing thick films is increasingly difficult as  $x$  decreases and

the lattice mismatch increases. A key enabler of thicker fully commensurate  $\alpha$ -(Al<sub>x</sub>Ga<sub>1-x</sub>)<sub>2</sub>O<sub>3</sub> films would be the existence of single crystal substrates or pseudosubstrates. There has been considerable progress on the growth of  $\beta$ -(Al<sub>x</sub>Ga<sub>1-x</sub>)<sub>2</sub>O<sub>3</sub> single crystals,<sup>58–60</sup> and work toward pseudosubstrates<sup>61</sup> has occurred in recent years. Similar development of high-quality  $\alpha$ -(Al<sub>x</sub>Ga<sub>1-x</sub>)<sub>2</sub>O<sub>3</sub> single-crystal substrates or pseudosubstrates would help the community investigate the potential of ultra-high bandgap materials.

## SUPPLEMENTARY MATERIAL

The supplementary material contains the calculated partial pressures of Ga<sub>2</sub>O and Al<sub>2</sub>O, an example HAADF-STEM image of a layered film, additional characterization data for all films shown in this paper, and a line profile of the  $\alpha$ -(Al<sub>0.78</sub>Ga<sub>0.22</sub>)<sub>2</sub>O<sub>3</sub> film shown in Fig. 3. The additional characterization data for each film includes an isolated  $2\theta$  scan from 33°–40°, the rocking curves of the substrate and film, and the AFM scan.

## ACKNOWLEDGMENTS

We acknowledge the support from the AFOSR/AFRL ACCESS Center of Excellence under Award No. FA9550-18-1-0529. This work used the Cornell Center for Materials Research (CCMR) Shared Facilities, which is supported through the NSF MRSEC Program (Grant No. DMR-1719875). Substrate preparation was performed, in part, at the Cornell NanoScale Facility, a member of the National Nanotechnology Coordinated Infrastructure (NNCI), which is supported by the NSF (Grant No. NNCI-2025233). This work also made use of the Cornell Energy Systems Institute Shared Facilities partly sponsored by the NSF (Grant No. MRI DMR-1338010).

We also personally thank Steven Button for preparing all the substrates used in these experiments. We also thank Matt Barone for the guidance in growth and maintenance and Yorick Birkhölzer for the direction in characterization. We also thank Yongjin Cho for his recognition that insufficient rotation speed can lead to the formation of layers with varying composition. Finally, we thank Shun-Li Shang and Zi-Kui Li for providing the vapor pressure data used to make Fig. S1 of the supplementary material.

## AUTHOR DECLARATIONS

### Conflict of Interest

The authors K. A. and D. G. S. have been granted U.S. Patent No. 11,462,402 (4 October 2022) with the title “Suboxide Molecular-Beam Epitaxy and Related Structures.”

## Author Contributions

**Jacob Steele:** Conceptualization (equal); Data curation (lead); Formal analysis (lead); Investigation (lead); Methodology (lead); Validation (equal); Visualization (lead); Writing – original draft (lead); Writing – review & editing (equal). **Kathy Azizie:** Conceptualization (supporting); Data curation (supporting); Formal analysis

(supporting); Investigation (supporting); Methodology (supporting); Visualization (supporting); Writing – original draft (supporting); Writing – review & editing (supporting). **Naomi Pieczulewski:** Data curation (equal); Formal analysis (equal); Visualization (equal); Writing – original draft (equal). **Yunjo Kim:** Data curation (supporting); Formal analysis (supporting); Writing – review & editing (supporting). **Shin Mou:** Formal analysis (supporting); Writing – review & editing (supporting). **Thaddeus J. Asel:** Formal analysis (supporting); Writing – review & editing (supporting). **Adam T. Neal:** Data curation (supporting); Formal analysis (supporting); Writing – review & editing (supporting). **Debdeep Jena:** Formal analysis (supporting); Resources (supporting); Supervision (supporting); Writing – original draft (supporting); Writing – review & editing (supporting). **Huili G. Xing:** Resources (supporting); Supervision (supporting); Writing – review & editing (supporting). **David A. Muller:** Formal analysis (supporting); Resources (supporting); Supervision (supporting); Visualization (supporting); Writing – original draft (supporting). **Takeyoshi Onuma:** Data curation (supporting); Formal analysis (supporting); Resources (supporting); Visualization (supporting); Writing – original draft (supporting); Writing – review & editing (supporting). **Darrell G. Schlom:** Conceptualization (equal); Formal analysis (supporting); Funding acquisition (lead); Investigation (supporting); Methodology (supporting); Project administration (lead); Resources (lead); Supervision (lead); Validation (equal); Visualization (supporting); Writing – original draft (supporting); Writing – review & editing (supporting).

## DATA AVAILABILITY

The data that support the findings of this study are available within the article.

## REFERENCES

- R. Roy, V. G. Hill, and E. Osborn, “Polymorphism of Ga<sub>2</sub>O<sub>3</sub> and the system Ga<sub>2</sub>O<sub>3</sub>–H<sub>2</sub>O,” *J. Am. Chem. Soc.* **74**, 719–722 (1952).
- S. Stepanov, V. Nikolaev, V. Bougrov, and A. Romanov, “Gallium oxide: Properties and applications A review,” *Rev. Adv. Mater. Sci.* **44**, 63–86 (2016).
- S. J. Pearton, J. Yang, P. H. Cary, F. Ren, J. Kim, M. J. Tadjer, and M. A. Mastro, “A review of Ga<sub>2</sub>O<sub>3</sub> materials, processing, and devices,” *Appl. Phys. Rev.* **5**, 011301 (2018).
- M. Yan-Mei, C. Hai-Yong, Y. Kai-Feng, L. Min, C. Qi-Liang, L. Jing, and Z. Guang-Tian, “High-pressure and high-temperature behaviour of gallium oxide,” *Chin. Phys. Lett.* **25**, 1603 (2008).
- T. Matsumoto, M. Aoki, A. Kinoshita, and T. Aono, “Absorption and reflection of vapor grown single crystal platelets of  $\beta$ -Ga<sub>2</sub>O<sub>3</sub>,” *Jpn. J. Appl. Phys.* **13**, 1578 (1974).
- Z. Galazka, “Growth of bulk  $\beta$ -Ga<sub>2</sub>O<sub>3</sub> single crystals by the Czochralski method,” *J. Appl. Phys.* **131**, 031103 (2022).
- C. Janowitz, V. Scherer, M. Mohamed, A. Krapf, H. Dwelk, R. Manzke, Z. Galazka, R. Uecker, K. Irmscher, R. Fornari, M. Michling, D. Schmeißer, J. R. Weber, J. B. Varley, and C. G. V. d. Walle, “Experimental electronic structure of In<sub>2</sub>O<sub>3</sub> and Ga<sub>2</sub>O<sub>3</sub>,” *New J. Phys.* **13**, 085014 (2011).
- A. Kuramata, K. Koshi, S. Watanabe, Y. Yamaoka, T. Masui, and S. Yamakoshi, “High-quality  $\beta$ -Ga<sub>2</sub>O<sub>3</sub> single crystals grown by edge-defined film-fed growth,” *Jpn. J. Appl. Phys.* **55**, 1202A2 (2016).
- M. Higashiwaki, K. Sasaki, H. Murakami, Y. Kumagai, A. Koukitu, A. Kuramata, T. Masui, and S. Yamakoshi, “Recent progress in Ga<sub>2</sub>O<sub>3</sub> power devices,” *Semicond. Sci. Technol.* **31**, 034001 (2016).
- B. J. Baliga, *Fundamentals of Power Semiconductor Devices*, 2nd ed. (Springer, 2019), pp. 1–31.

- <sup>11</sup>O. A. Dicks, J. Cottom, A. L. Shluger, and V. V. Afanas'ev, "The origin of negative charging in amorphous  $\text{Al}_2\text{O}_3$  films: The role of native defects," *Nanotechnology* **30**, 205201 (2019).
- <sup>12</sup>R. Jinno, C. S. Chang, T. Onuma, Y. Cho, S.-T. Ho, D. Rowe, M. C. Cao, K. Lee, V. Protasenko, D. G. Schlom, D. A. Muller, H. G. Xing, and D. Jena, "Crystal orientation dictated epitaxy of ultrawide-bandgap 5.4 to 8.6-eV  $\alpha$ -(Al, Ga) $_2\text{O}_3$  on m-plane sapphire," *Sci. Adv.* **7**, eabd5891 (2021).
- <sup>13</sup>T. Oshima, T. Okuno, N. Arai, Y. Kobayashi, and S. Fujita, " $\beta$ - $\text{Al}_{2-x}\text{Ga}_{2-2x}\text{O}_3$  thin film growth by molecular beam epitaxy," *Jpn. J. Appl. Phys.* **48**, 070202 (2009).
- <sup>14</sup>J. Y. Tsao, S. Chowdhury, M. A. Hollis, D. Jena, N. M. Johnson, K. A. Jones, R. J. Kaplar, S. Rajan, C. G. Van de Walle, E. Bellotti, C. L. Chua, R. Collazo, M. E. Coltrin, J. A. Cooper, K. R. Evans, S. Graham, T. A. Grotjohn, E. R. Heller, M. Higashiwaki, M. S. Islam, P. W. Juodawlkis, M. A. Khan, A. D. Koehler, J. H. Leach, U. K. Mishra, R. J. Nemanich, R. C. N. Pilawa-Podgurski, J. B. Shealy, Z. Sitar, M. J. Tadjer, A. F. Witulski, M. Wraback, and J. A. Simmons, "Ultrawide-bandgap semiconductors: Research opportunities and challenges," *Adv. Electron. Mater.* **4**, 1600501 (2018).
- <sup>15</sup>K. Y. Cheng, "Development of molecular beam epitaxy technology for III-V compound semiconductor heterostructure devices," *J. Vac. Sci. Technol., A* **31**, 050814 (2013).
- <sup>16</sup>K. Ploog, "Molecular beam epitaxy of III-V compounds: Technology and growth process," *Annu. Rev. Mater. Sci.* **11**, 171-210 (1981).
- <sup>17</sup>K. Ploog, "Molecular beam epitaxy of III-V compounds: Application of MBE-grown films," *Annu. Rev. Mater. Sci.* **12**, 123-148 (1982).
- <sup>18</sup>H. Kroemer, "Nobel lecture: Quasielectric fields and band offsets: Teaching electrons new tricks," *Rev. Mod. Phys.* **73**, 783-793 (2001).
- <sup>19</sup>A. Y. Cho, "Film deposition by molecular-beam techniques," *J. Vac. Sci. Technol.* **8**, S31-S38 (1971).
- <sup>20</sup>J. Arthur, "Molecular beam epitaxy," *Surf. Sci.* **500**, 189-217 (2002).
- <sup>21</sup>M. A. Herman and H. Sitter, *Molecular Beam Epitaxy: Fundamentals and Current Status* (Springer, Berlin, 1996), pp. 1-31.
- <sup>22</sup>A. F. M. Anhar Uddin Bhuiyan, Z. Feng, J. M. Johnson, Z. Chen, H.-L. Huang, J. Hwang, and H. Zhao, "MOCVD epitaxy of  $\beta$ -( $\text{Al}_x\text{Ga}_{1-x}$ ) $_2\text{O}_3$  thin films on (010)  $\text{Ga}_2\text{O}_3$  substrates and N-type doping," *Appl. Phys. Lett.* **115**, 120602 (2019).
- <sup>23</sup>A. F. M. Anhar Uddin Bhuiyan, Z. Feng, J. M. Johnson, H.-L. Huang, J. Hwang, and H. Zhao, "MOCVD epitaxy of ultrawide bandgap  $\beta$ -( $\text{Al}_x\text{Ga}_{1-x}$ ) $_2\text{O}_3$  with high-Al composition on (100)  $\beta$ - $\text{Ga}_2\text{O}_3$  substrates," *Cryst. Growth Des.* **20**, 6722-6730 (2020).
- <sup>24</sup>R. Kumaran, T. Tiedje, S. E. Webster, S. Penson, and W. Li, "Epitaxial Nd-doped  $\alpha$ -( $\text{Al}_x\text{Ga}_{1-x}$ ) $_2\text{O}_3$  films on sapphire for solid-state waveguide lasers," *Opt. Lett.* **35**, 3793-3795 (2010).
- <sup>25</sup>J. P. McCandless, C. S. Chang, K. Nomoto, J. Casamento, V. Protasenko, P. Vogt, D. Rowe, K. Gann, S. T. Ho, W. Li, R. Jinno, Y. Cho, A. J. Green, K. D. Chabak, D. G. Schlom, M. O. Thompson, D. A. Muller, H. G. Xing, and D. Jena, "Thermal stability of epitaxial  $\alpha$ - $\text{Ga}_2\text{O}_3$  and (Al, Ga) $_2\text{O}_3$  layers on m-plane sapphire," *Appl. Phys. Lett.* **119**, 062102 (2021).
- <sup>26</sup>R. Schewski, G. Wagner, M. Baldini, D. Gogova, Z. Galazka, T. Schulz, T. Remele, T. Markurt, H. von Wenckstern, M. Grundmann, O. Bierwagen, P. Vogt, and M. Albrecht, "Epitaxial stabilization of pseudomorphic  $\text{Ga}_2\text{O}_3$  on sapphire (0001)," *Appl. Phys. Express* **8**, 011101 (2014).
- <sup>27</sup>H. Akazawa, "Formation of various phases of gallium oxide films depending on substrate planes and deposition gases," *Vacuum* **123**, 8-16 (2016).
- <sup>28</sup>D. Shinohara and S. Fujita, "Heteroepitaxy of corundum-structured  $\alpha$ - $\text{Ga}_2\text{O}_3$  thin films on  $\alpha$ - $\text{Al}_2\text{O}_3$  substrates by ultrasonic mist chemical vapor deposition," *Jpn. J. Appl. Phys.* **47**, 7311 (2008).
- <sup>29</sup>Y. Oshima, E. G. Villora, and K. Shimamura, "Halide vapor phase epitaxy of twin-free  $\alpha$ - $\text{Ga}_2\text{O}_3$  on sapphire (0001) substrates," *Appl. Phys. Express* **8**, 055501 (2015).
- <sup>30</sup>Y. Yao, S. Okur, L. A. M. Lyle, G. S. Tompa, T. Salagaj, N. Sbrockey, R. F. Davis, and L. M. Porter, "Growth and characterization of  $\alpha$ - $\beta$ - and  $\epsilon$ -phases of  $\text{Ga}_2\text{O}_3$  using MOCVD and HVPE techniques," *Mater. Res. Lett.* **6**, 268-275 (2018).
- <sup>31</sup>P. Vogt and O. Bierwagen, "Reaction kinetics and growth window for plasma-assisted molecular beam epitaxy of  $\text{Ga}_2\text{O}_3$ : Incorporation of Ga vs.  $\text{Ga}_2\text{O}$  desorption," *Appl. Phys. Lett.* **108**, 072101 (2016).
- <sup>32</sup>P. Vogt, O. Brandt, H. Riechert, J. Lähnemann, and O. Bierwagen, "Metal-exchange catalysis in the growth of sesquioxides: Towards heterostructures of transition oxide semiconductors," *Phys. Rev. Lett.* **119**, 196001 (2017).
- <sup>33</sup>M.-Y. Tsai, O. Bierwagen, M. E. White, and J. S. Speck, " $\beta$ - $\text{Ga}_2\text{O}_3$  growth by plasma-assisted molecular beam epitaxy," *J. Vac. Sci. Technol., A* **28**, 354-359 (2010).
- <sup>34</sup>J. P. McCandless, V. Protasenko, B. W. Morell, E. Steinbrunner, A. T. Neal, N. Tanen, Y. Cho, T. J. Asel, S. Mou, P. Vogt, H. G. Xing, and D. Jena, "Controlled Si doping of  $\beta$ - $\text{Ga}_2\text{O}_3$  by molecular beam epitaxy," *Appl. Phys. Lett.* **121**, 072108 (2022).
- <sup>35</sup>S. Migita, Y. Kasai, H. Ota, and S. Sakai, "Self-limiting process for the bismuth content in molecular beam epitaxial growth of  $\text{Bi}_2\text{Sr}_2\text{CuO}_7$  thin films," *Appl. Phys. Lett.* **71**, 3712-3714 (1997).
- <sup>36</sup>R. W. Ulbricht, A. Schmehl, T. Heeg, J. Schubert, and D. G. Schlom, "Adsorption-controlled growth of EuO by molecular-beam epitaxy," *Appl. Phys. Lett.* **93**, 102105 (2008).
- <sup>37</sup>J. L. MacManus-Driscoll, M. P. Wells, C. Yun, J.-W. Lee, C.-B. Eom, and D. G. Schlom, "New approaches for achieving more perfect transition metal oxide thin films," *APL Mater.* **8**, 040904 (2020).
- <sup>38</sup>O. Bierwagen, M. E. White, M.-Y. Tsai, and J. S. Speck, "Plasma-assisted molecular beam epitaxy of high quality  $\text{In}_2\text{O}_3$  (001) thin films on Y-stabilized  $\text{ZrO}_2$ (001) using in as an auto surfactant," *Appl. Phys. Lett.* **95**, 262105 (2009).
- <sup>39</sup>H. Paik, Z. Chen, E. Lochocki, A. Seidner H., A. Verma, N. Tanen, J. Park, M. Uchida, S. Shang, B.-C. Zhou, M. Brützmam, R. Uecker, Z.-K. Liu, D. Jena, K. M. Shen, D. A. Muller, and D. G. Schlom, "Adsorption-controlled growth of La-doped  $\text{BaSnO}_3$  by molecular-beam epitaxy," *APL Mater.* **5**, 116107 (2017).
- <sup>40</sup>A. B. Mei, L. Miao, M. J. Wahila, G. Khalsa, Z. Wang, M. Barone, N. J. Schreiber, L. E. Noskin, H. Paik, T. E. Tiwald, Q. Zheng, R. T. Haasch, D. G. Sangiovanni, L. F. J. Piper, and D. G. Schlom, "Adsorption-controlled growth and properties of epitaxial  $\text{SnO}$  films," *Phys. Rev. Materials* **3**, 105202 (2019).
- <sup>41</sup>E. Korhonen, F. Tuomisto, D. Gogova, G. Wagner, M. Baldini, Z. Galazka, R. Schewski, and M. Albrecht, "Electrical compensation by Ga vacancies in  $\text{Ga}_2\text{O}_3$  thin films," *Appl. Phys. Lett.* **106**, 242103 (2015).
- <sup>42</sup>H. Peelaers, J. B. Varley, J. S. Speck, and C. G. Van de Walle, "Appl. Phys. Lett." **112**, 242101 (2018).
- <sup>43</sup>P. Vogt, F. V. E. Hensling, K. Azizie, C. S. Chang, D. Turner, J. Park, J. P. McCandless, H. Paik, B. J. Bocklund, G. Hoffman, O. Bierwagen, D. Jena, H. G. Xing, S. Mou, D. A. Muller, S.-L. Shang, Z.-K. Liu, and D. G. Schlom, "Adsorption-controlled growth of  $\text{Ga}_2\text{O}_3$  by suboxide molecular-beam epitaxy," *APL Mater.* **9**, 031101 (2021).
- <sup>44</sup>K. Azizie, F. V. E. Hensling, C. A. Gorsak, Y. Kim, N. A. Pieczulewski, D. M. Dryden, M. K. I. Senevirathna, S. Coye, S.-L. Shang, J. Steele, P. Vogt, N. A. Parker, Y. A. Birkhölzer, J. P. McCandless, D. Jena, H. G. Xing, Z.-K. Liu, M. D. Williams, A. J. Green, K. Chabak, D. A. Muller, A. T. Neal, S. Mou, M. O. Thompson, H. P. Nair, and D. G. Schlom, "Silicon-doped  $\beta$ - $\text{Ga}_2\text{O}_3$  films grown at 1  $\mu\text{m}/\text{h}$  by suboxide molecular-beam epitaxy," *APL Mater.* **11**, 041102 (2023).
- <sup>45</sup>T. J. Smart, F. V. E. Hensling, D. Y. Kim, L. N. Majer, Y. E. Suyolcu, D. Dereh, D. G. Schlom, D. Jena, J. Mannhart, and W. Braun, "Why thermal laser epitaxy aluminum sources yield reproducible fluxes in oxidizing environments," *J. Vac. Sci. Technol., A* **41**, 042701 (2023).
- <sup>46</sup>S.-L. Shang, S. Lin, M. C. Gao, D. G. Schlom, and Z.-K. Liu, "Ellingham Diagrams of Binary Oxides," *arXiv:2308.05837* (2023).
- <sup>47</sup>J. Roberts, J. Jarman, D. Johnstone, P. Midgley, P. Chalker, R. Oliver, and F.-P. Massabuau, " $\alpha$ - $\text{Ga}_2\text{O}_3$  grown by low temperature atomic layer deposition on sapphire," *J. Cryst. Growth* **487**, 23-27 (2018).
- <sup>48</sup>M. Kracht, A. Karg, M. Feneberg, J. Bläsing, J. Schörmann, R. Goldhahn, and M. Eickhoff, "Anisotropic optical properties of metastable (01 $\bar{1}2$ )  $\alpha$ - $\text{Ga}_2\text{O}_3$  grown by plasma-assisted molecular beam epitaxy," *Phys. Rev. Appl.* **10**, 024047 (2018).
- <sup>49</sup>L. Majer, S. Smink, P. Vogt, H. Wang, K. S. Rabinovich, T. Acartürk, J. Steele, J. L. Eckl-Haese, D. G. Schlom, U. Starke, A. Boris, P. A. van Aken, J. Mannhart, W. Braun, and F. V. Hensling, "Adsorption-controlled homoepitaxial growth of C-plane sapphire" (unpublished).
- <sup>50</sup>K. Robbie, M. J. Brett, and A. Lakhtakia, "Chiral sculptured thin films," *Nature* **384**, 616 (1996).

- <sup>51</sup>A. Miller, M. Lemon, M. Choffel, S. Rich, F. Harvel, and D. Johnson, "Extracting information from X-ray diffraction patterns containing Laue oscillations," *Z. Naturforsch., B: J. Chem.* **77**, 313–322 (2022).
- <sup>52</sup>L. Vegard, "Die Konstitution der Mischkristalle und die Raumfüllung der atome," *Z. Phys.* **5**, 17–26 (1921).
- <sup>53</sup>G. T. Dang, T. Yasuoka, Y. Tagashira, T. Tadokoro, W. Theiss, and T. Kawaharamura, "Bandgap engineering of  $\alpha$ -(Al<sub>x</sub>Ga<sub>1-x</sub>)<sub>2</sub>O<sub>3</sub> by a mist chemical vapor deposition two-chamber system and verification of Vegard's law," *Appl. Phys. Lett.* **113**, 062102 (2018).
- <sup>54</sup>J. Neave, P. Dobson, B. Joyce, and J. Zhang, "Reflection high-energy electron diffraction oscillations from vicinal surfaces—a new approach to surface diffusion measurements," *Appl. Phys. Lett.* **47**, 100–102 (1985).
- <sup>55</sup>A. Segura, L. Artús, R. Cuscó, R. Goldhahn, and M. Feneberg, "Band gap of corundumlike  $\alpha$ -Ga<sub>2</sub>O<sub>3</sub> determined by absorption and ellipsometry," *Phys. Rev. Mater.* **1**, 024604 (2017).
- <sup>56</sup>M. Hilfiker, R. Korlacki, R. Jinno, Y. Cho, H. G. Xing, D. Jena, U. Kilic, M. Stokey, and M. Schubert, "Anisotropic dielectric functions, band-to-band transitions, and critical points in  $\alpha$ -Ga<sub>2</sub>O<sub>3</sub>," *Appl. Phys. Lett.* **118**, 062103 (2021).
- <sup>57</sup>D. Wickramaratne, J. B. Varley, and J. L. Lyons, "Donor doping of corundum (Al<sub>x</sub>Ga<sub>1-x</sub>)<sub>2</sub>O<sub>3</sub>," *Appl. Phys. Lett.* **121**, 042110 (2022).
- <sup>58</sup>D. Bauman, D. I. Panov, D. A. Zakgeim, V. Spiridonov, A. V. Kremleva, A. A. Petrenko, P. N. Brunkov, N. D. Prasolov, A. V. Nashchekin, A. M. Smirnov, M. A. Odnoblyudov, V. E. Bougrov, and A. E. Romanov, "High-quality bulk  $\beta$ -Ga<sub>2</sub>O<sub>3</sub> and  $\beta$ -(Al<sub>x</sub>Ga<sub>1-x</sub>)<sub>2</sub>O<sub>3</sub> crystals: Growth and properties," *Phys. Status Solidi A* **218**, 2100335 (2021).
- <sup>59</sup>J. Jesenovec, B. Dutton, N. Stone-Weiss, A. Chmielewski, M. Saleh, C. Peterson, N. Alem, S. Krishnamoorthy, and J. S. McCloy, "Alloyed  $\beta$ -(Al<sub>x</sub>Ga<sub>1-x</sub>)<sub>2</sub>O<sub>3</sub> bulk Czochralski single  $\beta$ -(Al<sub>0.1</sub>Ga<sub>0.9</sub>)<sub>2</sub>O<sub>3</sub> and polycrystals  $\beta$ -(Al<sub>0.33</sub>Ga<sub>0.66</sub>)<sub>2</sub>O<sub>3</sub>,  $\beta$ -(Al<sub>0.5</sub>Ga<sub>0.5</sub>)<sub>2</sub>O<sub>3</sub>, and property trends," *J. Appl. Phys.* **131**, 155702 (2022).
- <sup>60</sup>Z. Galazka, A. Fiedler, A. Popp, S. Ganschow, A. Kwasniewski, P. Seyidov, M. Pietsch, A. Dittmar, S. B. Anooz, K. Irmscher, M. Suendermann, D. Klimm, T.-S. Chou, J. Rehm, T. Schroeder, and M. Bickermann, "Bulk single crystals and physical properties of  $\beta$ -(Al<sub>x</sub>Ga<sub>1-x</sub>)<sub>2</sub>O<sub>3</sub> (x = 0–0.35) grown by the Czochralski method," *J. Appl. Phys.* **133**, 035702 (2023).
- <sup>61</sup>D. Yang, B. Kim, T. H. Lee, J. Oh, S. Lee, W. Sohn, E. Yoon, Y. Park, and H. W. Jang, "Selective area growth of single-crystalline alpha-gallium oxide on a sapphire nanomembrane by mist chemical vapor deposition," *ACS Appl. Electron. Mater.* **3**, 4328–4336 (2021).

**Supplementary Material for "Epitaxial Growth of  $\alpha$ -(Al<sub>x</sub>Ga<sub>1-x</sub>)<sub>2</sub>O<sub>3</sub> at 1  $\mu$ m/h"**

Jacob Steele,<sup>1</sup> Kathy Azizie,<sup>1</sup> Naomi Pieczulewski,<sup>1</sup> Yunjo Kim,<sup>2</sup> Shin Mou,<sup>2</sup> Thaddeus J. Asel,<sup>2</sup> Adam T. Neal,<sup>2</sup> Debdeep Jena,<sup>1,3,4</sup> Huili G. Xing,<sup>1,3,4</sup> David A. Muller,<sup>5,3</sup> Takeyoshi Onuma,<sup>6</sup> and Darrell. G. Schlom<sup>1,3,7</sup>

<sup>1</sup>*Department of Materials Science and Engineering, Cornell University, Ithaca 14853, New York, USA*

<sup>2</sup>*Air Force Research Lab, Materials and Manufacturing Directorate, Wright Patterson AFB, Ohio 45433, USA*

<sup>3</sup>*Kavli Institute at Cornell for Nanoscale Science, Ithaca, 14853, New York, USA*

<sup>4</sup>*Department of Electrical and Computer Engineering, Cornell University, Ithaca 14853, New York, USA*

<sup>5</sup>*School of Applied and Engineering Physics, Cornell University, Ithaca 14853, New York, USA*

<sup>6</sup>*Department of Applied Physics, Kogakuin University, 2665-1 Hachioji, Tokyo 192-0015, Japan*

<sup>7</sup>*Leibniz-Institut für Kristallzüchtung, Max-Born-Str. 2, 12489 Berlin, Germany*

(Dated: 12 March 2024)

I. SUPPLEMENTAL

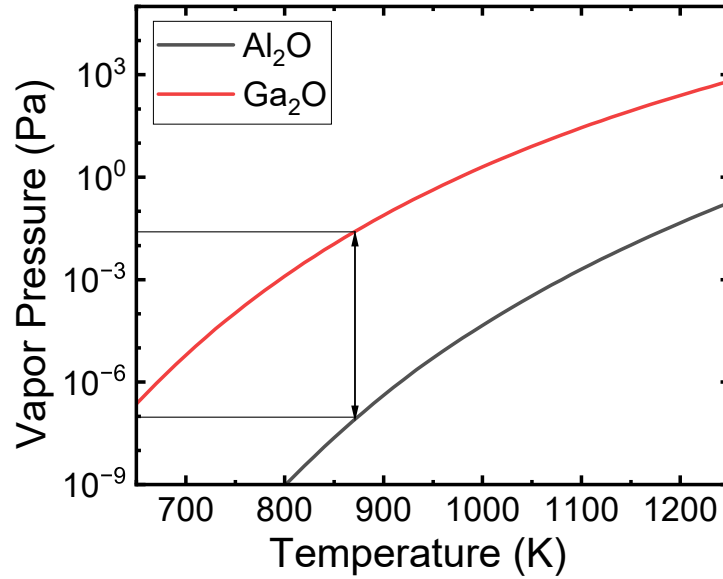


FIG. S1. Vapor pressures of  $\text{Al}_2\text{O}$  and  $\text{Ga}_2\text{O}$  in Pa over the range of 650 K - 1250 K with the background pressure of  $\text{O}_2$  held at  $10^{-4}$  Pa ( $7.5 \times 10^{-7}$  Torr). The calculated partial pressures are over the source mixtures of  $\text{Me}_2\text{O}_3(\text{s}) + \text{Me}(\text{L})$  with  $\text{Me} = \text{Al}$  and  $\text{Ga}$  for  $\text{Al}_2\text{O}$  and  $\text{Ga}_2\text{O}$ , respectively. The arrow marks the average growth temperature of the films in this paper, 605 °C. At this temperature, the vapor pressure of  $\text{Ga}_2\text{O}$  is over  $10^5$  times higher than  $\text{Al}_2\text{O}$ , confirming that  $\text{Ga}_2\text{O}$  is significantly more volatile.

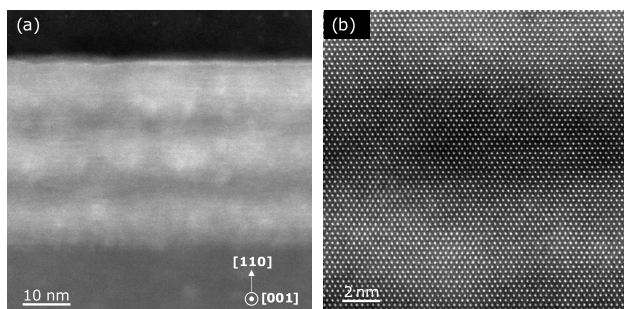


FIG. S2. HAADF-STEM image of an  $\alpha$ -(Al<sub>0.80</sub>Ga<sub>0.20</sub>)<sub>2</sub>O<sub>3</sub> film grown for 1 minute with a rotation speed of 3 rotations per minute, which results in 3 distinct layers of composition. An increase in intensity correlates with regions of higher gallium incorporation. The oscillations occur with a period equal to the substrate rotations due to the high growth rates allowing many monolayers to grow before a full rotation can occur. Since the sources do not have a perfectly even flux distribution across the film surface this leads to changes in composition as the film rotates. This method can be utilized to grow chiral, layered structures with highly controllable layer thicknesses by altering the rotation speed and growth rate.

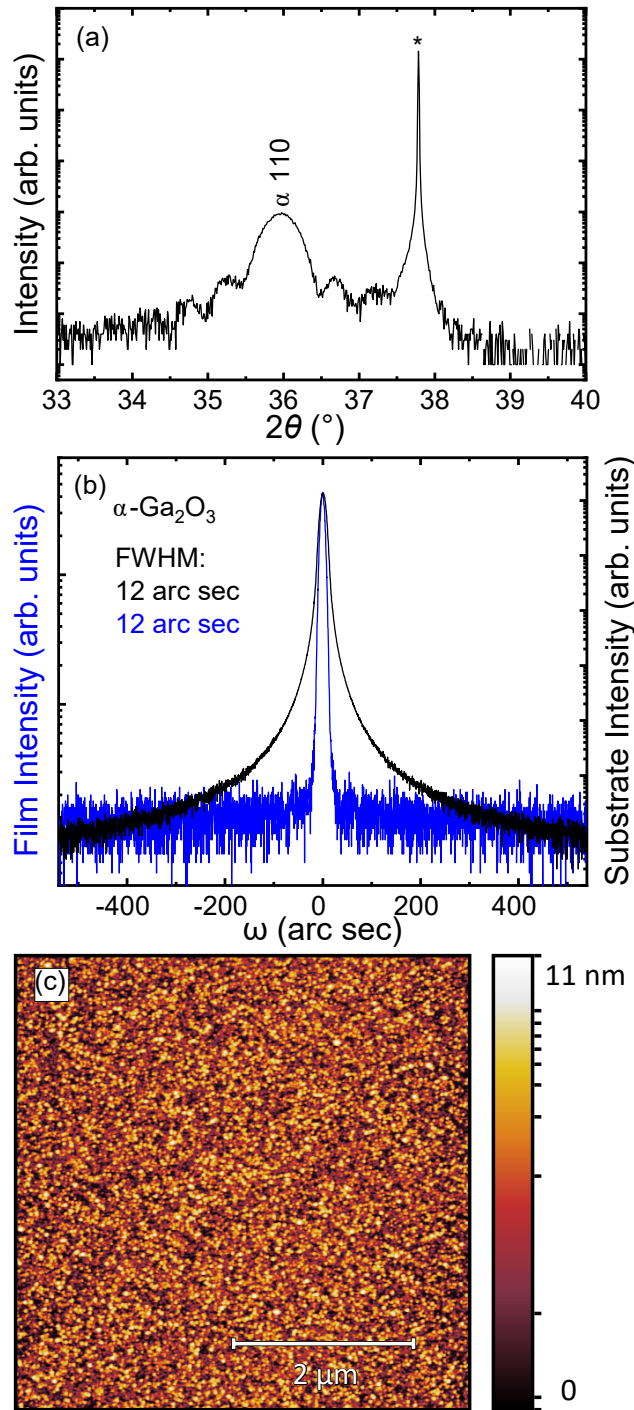


FIG. S3. (a): XRD plot of the  $\alpha$ -Ga<sub>2</sub>O<sub>3</sub> film over the range of  $2\theta = 33^\circ - 40^\circ$ . (b): The rocking curve of the film, shown in blue, has a FWHM of 12 arc sec. The rocking curve of the substrate, shown in black, is given as a comparison for the film and has a FWHM of 12 arc sec. (c): AFM shows that the growth surface has a RMS roughness of 1.06 nm on a thickness of 20.0 nm.

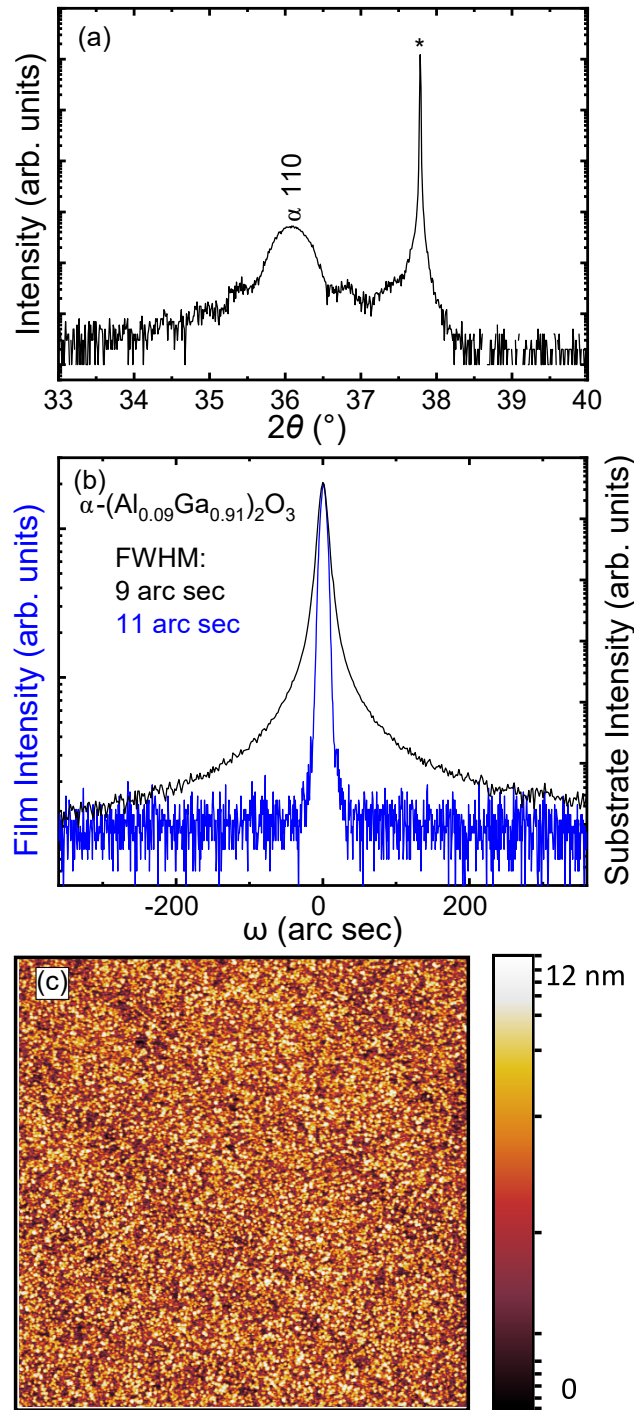


FIG. S4. (a): XRD plot of the  $\alpha$ -(Al<sub>0.09</sub>Ga<sub>0.91</sub>)<sub>2</sub>O<sub>3</sub> film over the range of  $2\theta = 33^\circ - 40^\circ$ . (b): The rocking curve of the film, shown in blue, has a FWHM of 11 arc sec. The rocking curve of the substrate, shown in black, is given as a comparison for the film and has a FWHM of 9 arc sec. (c): AFM shows that the growth surface has a RMS roughness of 1.13 nm on a thickness of 20.3 nm.

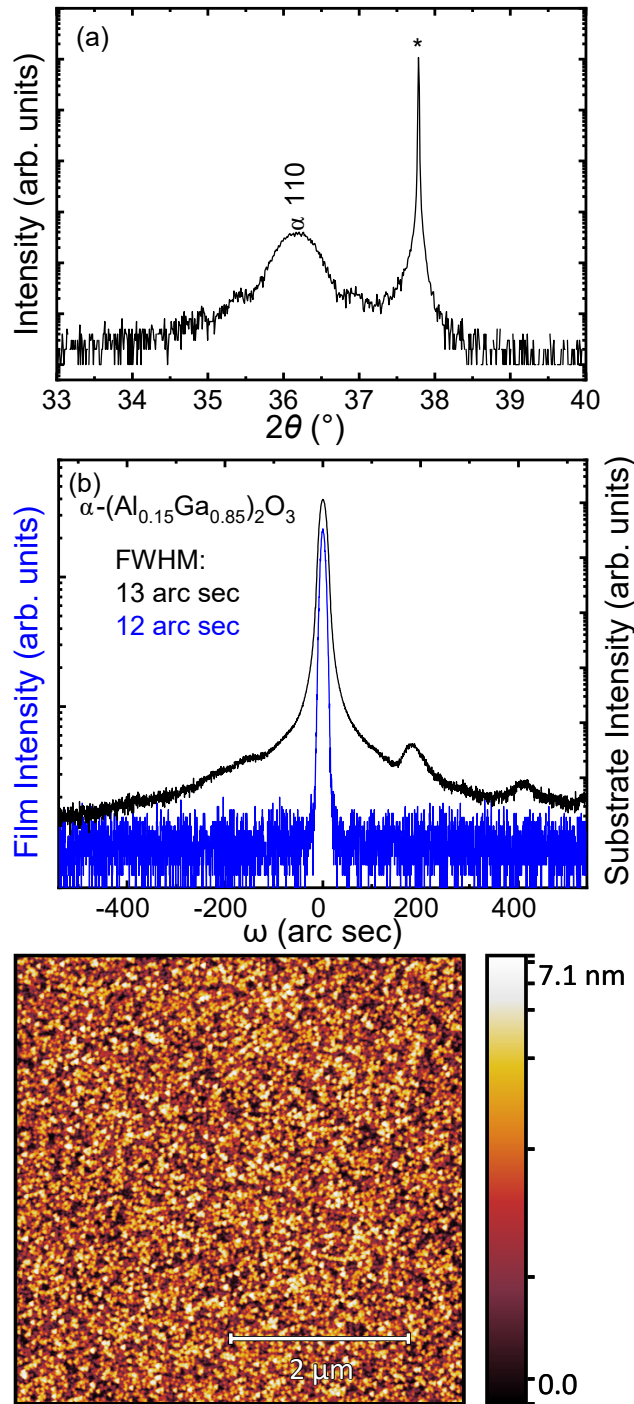


FIG. S5. (a): XRD plot of the  $\alpha$ -(Al<sub>0.15</sub>Ga<sub>0.85</sub>)<sub>2</sub>O<sub>3</sub> film over the range of  $2\theta = 33^\circ - 40^\circ$ . (b): The rocking curve of the film, shown in blue, has a FWHM of 12 arc sec. The rocking curve of the substrate, shown in black, is given as a comparison for the film and has a FWHM of 13 arc sec. (c): AFM shows that the growth surface has a RMS roughness of 1.01 nm on a thickness of 19.2 nm.

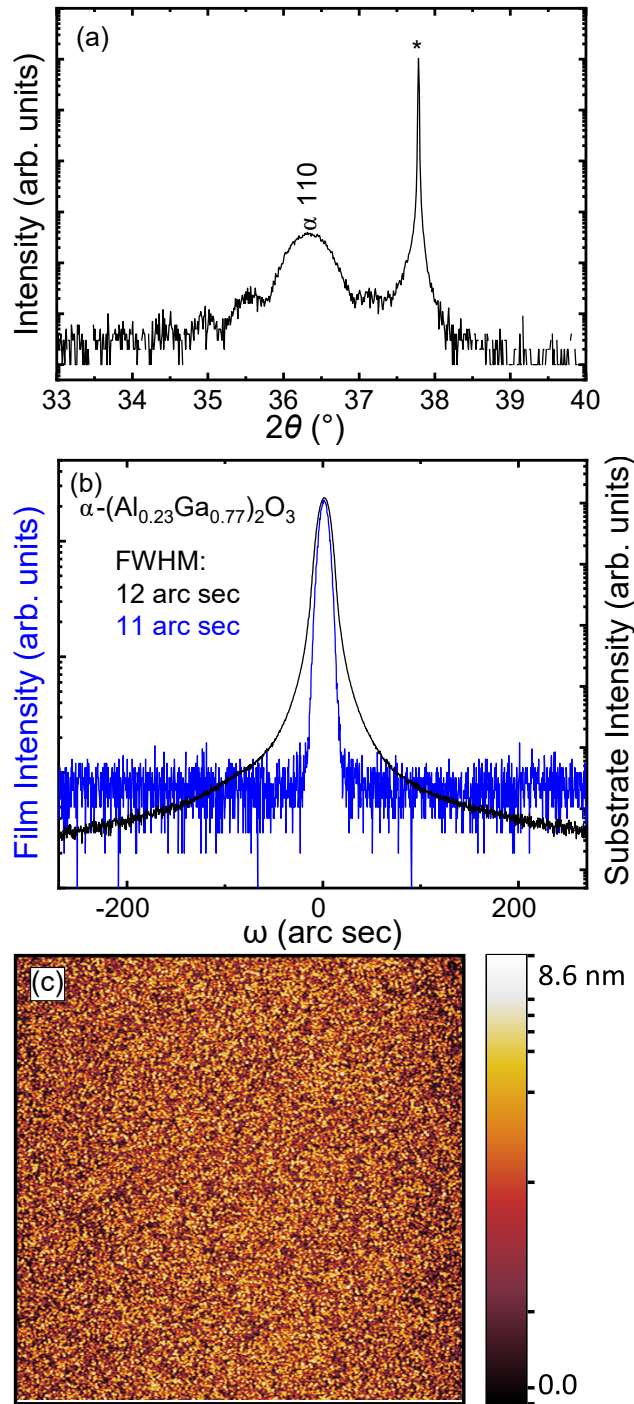


FIG. S6. (a): XRD plot of the  $\alpha$ -(Al<sub>0.23</sub>Ga<sub>0.77</sub>)<sub>2</sub>O<sub>3</sub> film over the range of  $2\theta = 33^\circ - 40^\circ$ . (b): The rocking curve of the film, shown in blue, has a FWHM of 11 arc sec. The rocking curve of the substrate, shown in black, is given as a comparison for the film and has a FWHM of 12 arc sec. (c): AFM shows that the growth surface has a RMS roughness of 0.915 nm on a thickness of 17.8 nm.

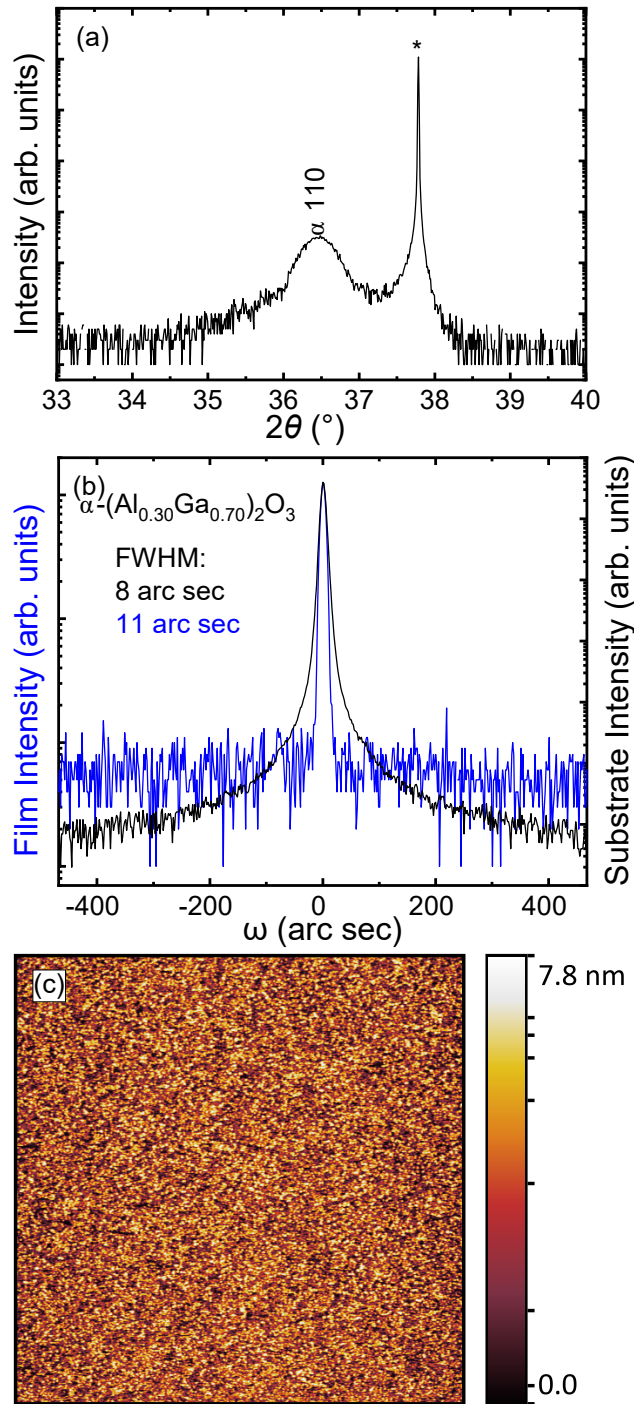


FIG. S7. (a): XRD plot of the  $\alpha$ -(Al<sub>0.30</sub>Ga<sub>0.70</sub>)<sub>2</sub>O<sub>3</sub> film over the range of  $2\theta = 33^\circ - 40^\circ$ . (b): The rocking curve of the film, shown in blue, has a FWHM of 11 arc sec. The rocking curve of the substrate, shown in black, is given as a comparison for the film and has a FWHM of 8 arc sec. (c): AFM shows that the growth surface has a RMS roughness of 0.970 nm on a thickness of 22.3 nm.

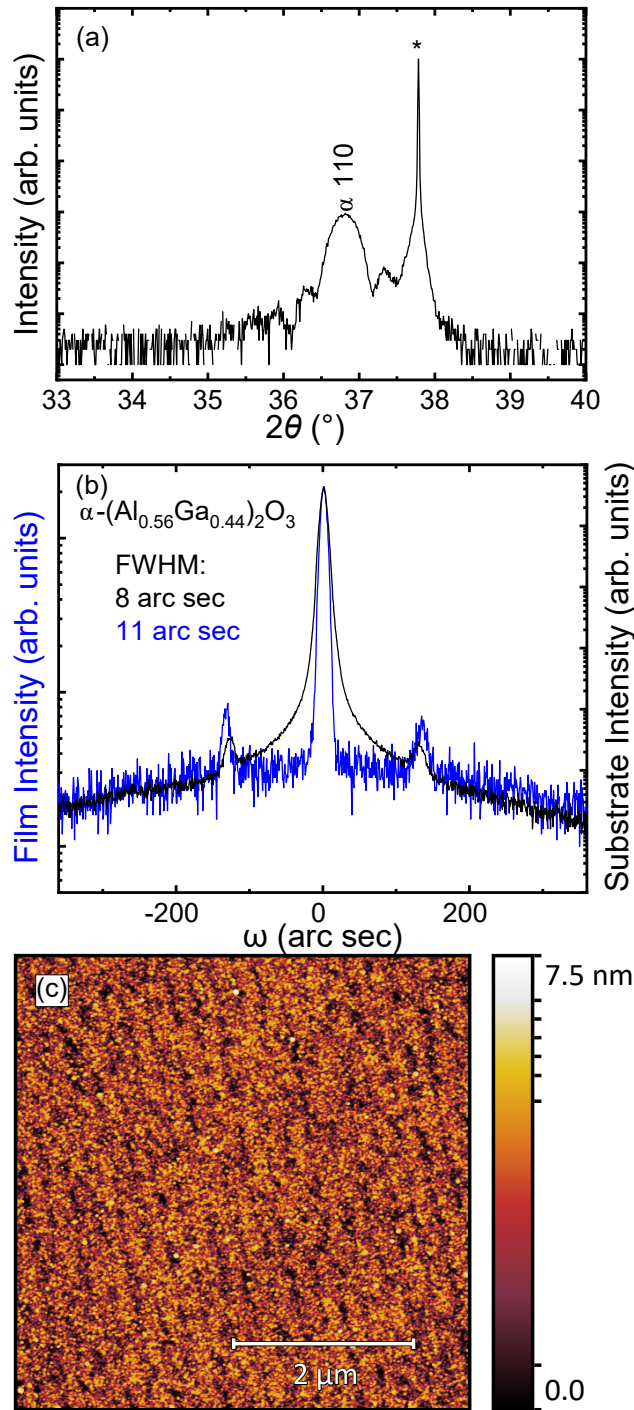


FIG. S8. (a): XRD plot of the  $\alpha$ -(Al<sub>0.56</sub>Ga<sub>0.44</sub>)<sub>2</sub>O<sub>3</sub> film over the range of  $2\theta = 33^\circ - 40^\circ$ . (b): The rocking curve of the film, shown in blue, has a FWHM of 11 arc sec. The rocking curve of the substrate, shown in black, is given as a comparison for the film and has a FWHM of 8 arc sec. (c): AFM shows that the growth surface has a RMS roughness of 0.326 nm on a thickness of 27.3 nm.

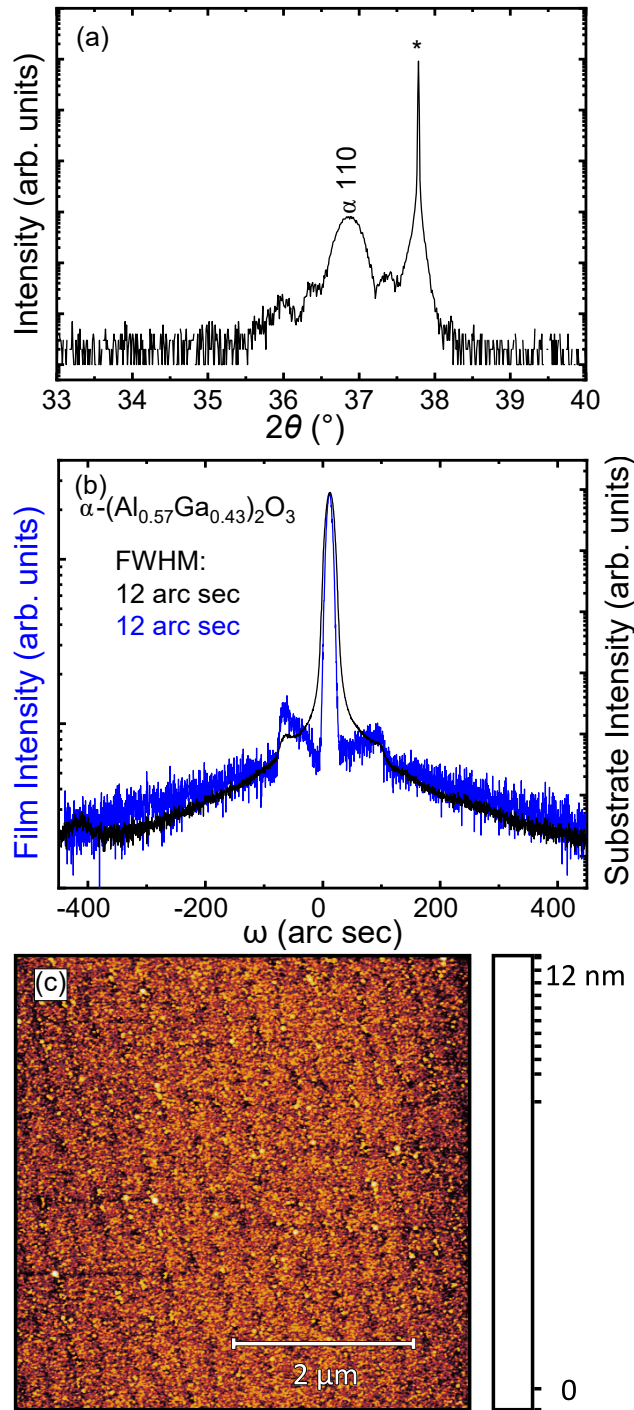


FIG. S9. (a): XRD plot of the  $\alpha$ -(Al<sub>0.57</sub>Ga<sub>0.43</sub>)<sub>2</sub>O<sub>3</sub> film over the range of  $2\theta = 33^\circ - 40^\circ$ . (b): The rocking curve of the film, shown in blue, has a FWHM of 12 arc sec. The rocking curve of the substrate, shown in black, is given as a comparison for the film and has a FWHM of 12 arc sec. (c): AFM shows that the growth surface has a RMS roughness of 0.409 nm on a thickness of 29.0 nm.

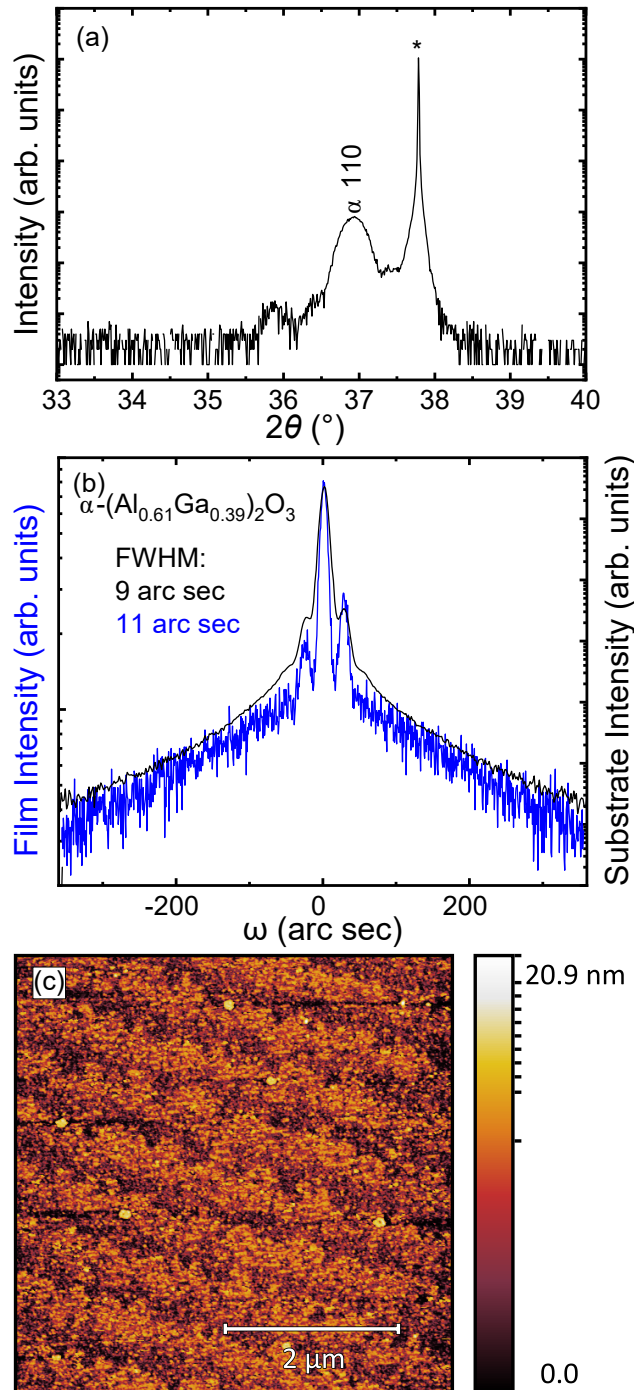


FIG. S10. (a): XRD plot of the  $\alpha$ -(Al<sub>0.61</sub>Ga<sub>0.39</sub>)<sub>2</sub>O<sub>3</sub> film over the range of  $2\theta = 33^\circ - 40^\circ$ . (b): The rocking curve of the film, shown in blue, has a FWHM of 11 arc sec. The rocking curve of the substrate, shown in black, is given as a comparison for the film and has a FWHM of 9 arc sec. (c): AFM shows that the growth surface has a RMS roughness of 0.646 nm on a thickness of 30.2 nm.

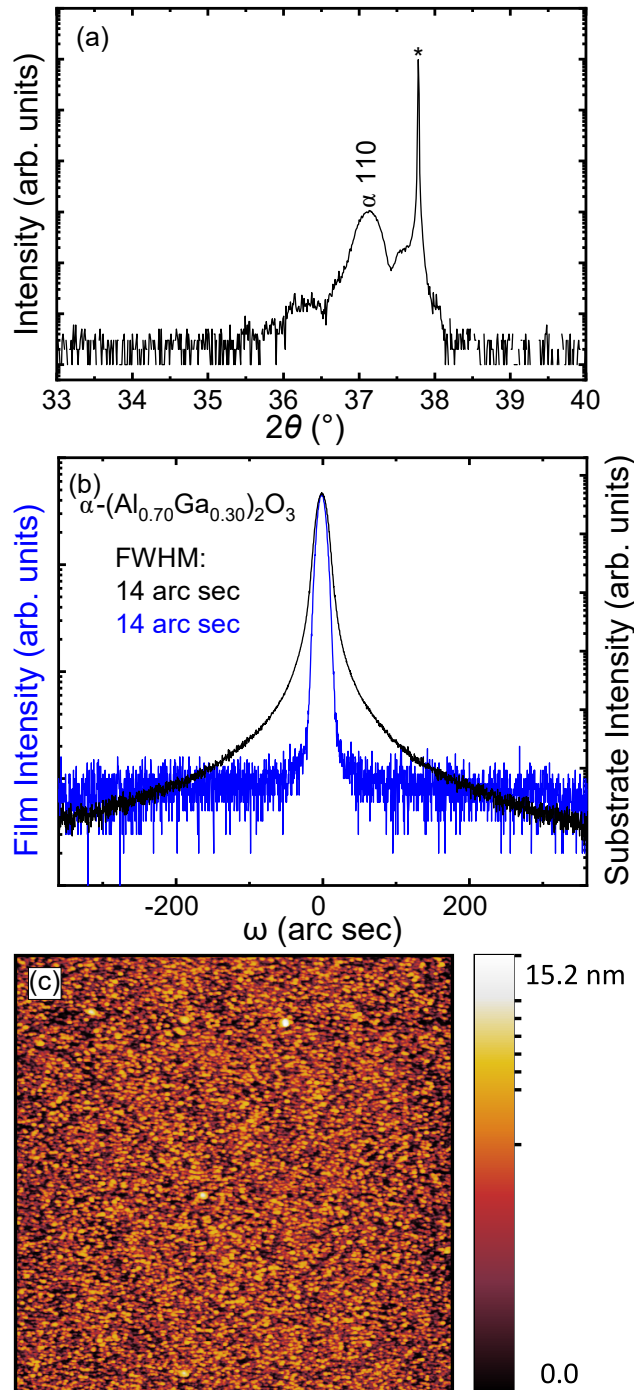


FIG. S11. (a): XRD plot of the  $\alpha$ -(Al<sub>0.70</sub>Ga<sub>0.30</sub>)<sub>2</sub>O<sub>3</sub> film over the range of  $2\theta = 33^\circ - 40^\circ$ . (b): The rocking curve of the film, shown in blue, has a FWHM of 14,arc sec. The rocking curve of the substrate, shown in black, is given as a comparison for the film and has a FWHM of 14 arc sec. (c): AFM shows that the growth surface has a RMS roughness of 0.543 nm on a thickness of 32.5 nm.

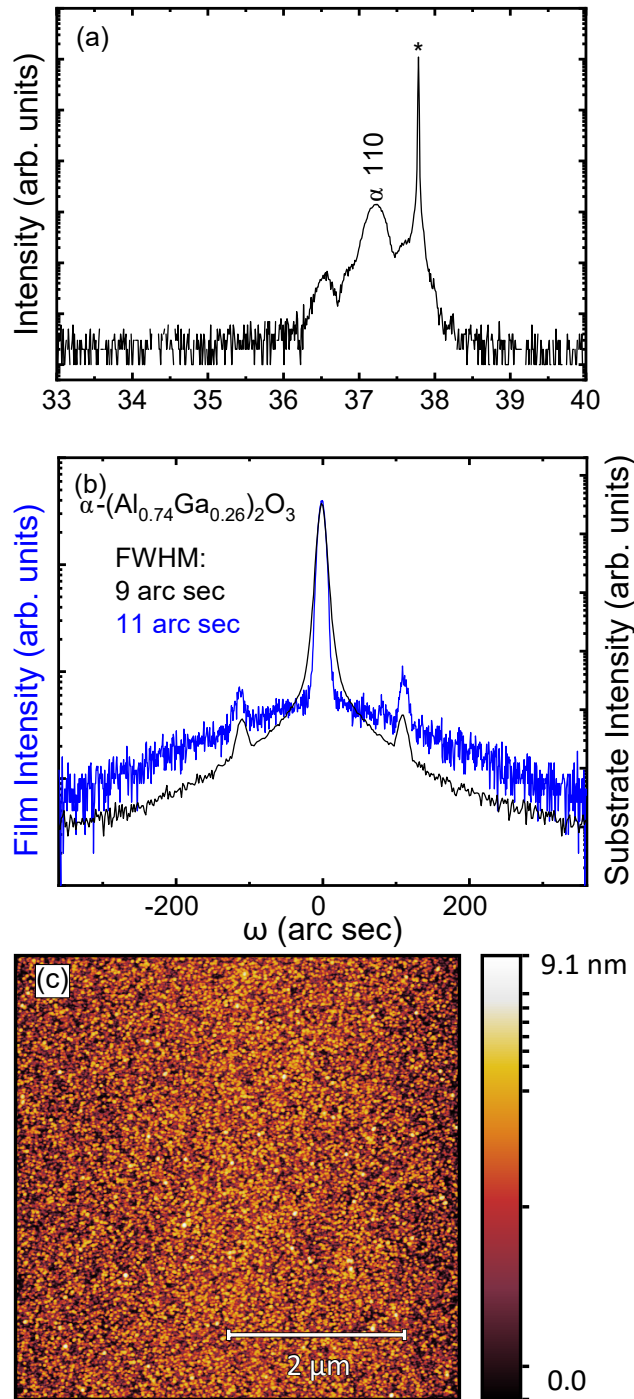


FIG. S12. (a): XRD plot of the  $\alpha$ -(Al<sub>0.74</sub>Ga<sub>0.26</sub>)<sub>2</sub>O<sub>3</sub> film over the range of  $2\theta = 33^\circ - 40^\circ$ . (b): The rocking curve of the film, shown in blue, has a FWHM of 11 arc sec. The rocking curve of the substrate, shown in black, is given as a comparison for the film and has a FWHM of 9 arc sec. (c): AFM shows that the growth surface has a RMS roughness of 0.551 nm on a thickness of 39.3 nm.

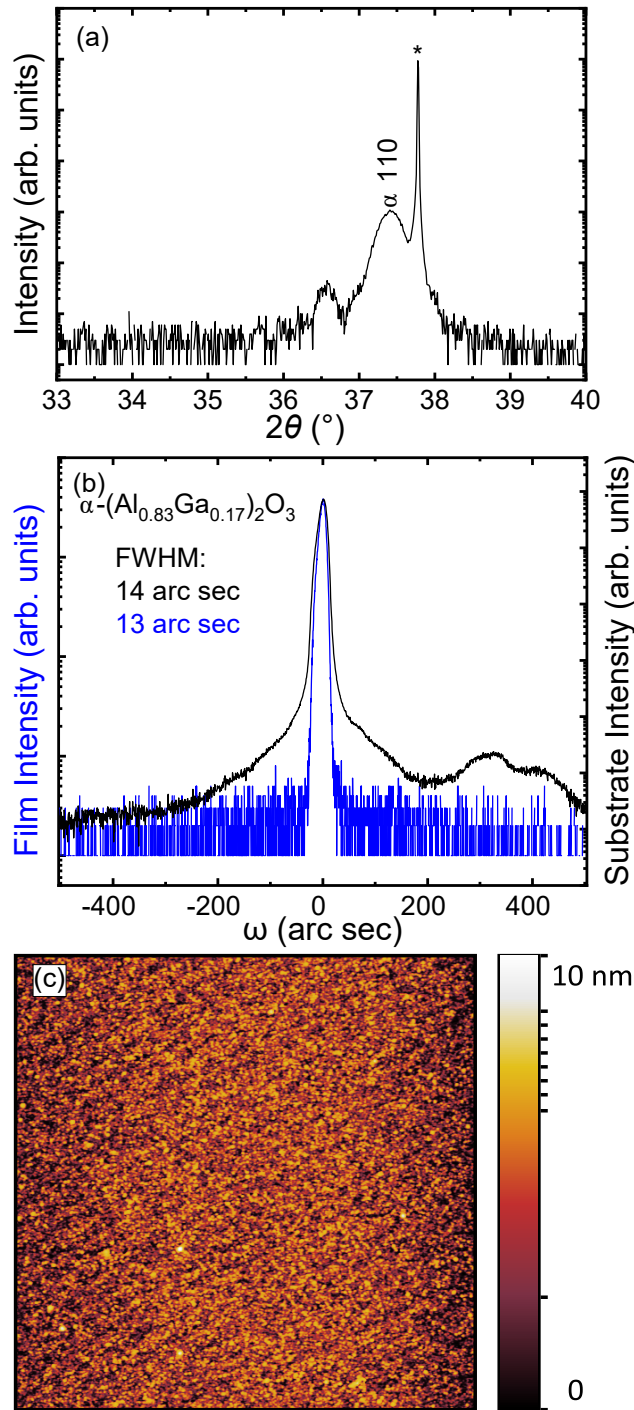


FIG. S13. (a): XRD plot of the  $\alpha$ -(Al<sub>0.83</sub>Ga<sub>0.17</sub>)<sub>2</sub>O<sub>3</sub> film over the range of  $2\theta = 33^\circ - 40^\circ$ . (b): The rocking curve of the film, shown in blue, has a FWHM of 13 arc sec. The rocking curve of the substrate, shown in black, is given as a comparison for the film and has a FWHM of 14 arc sec. (c): AFM shows that the growth surface has a RMS roughness of 0.308 nm on a thickness of 33.5 nm.

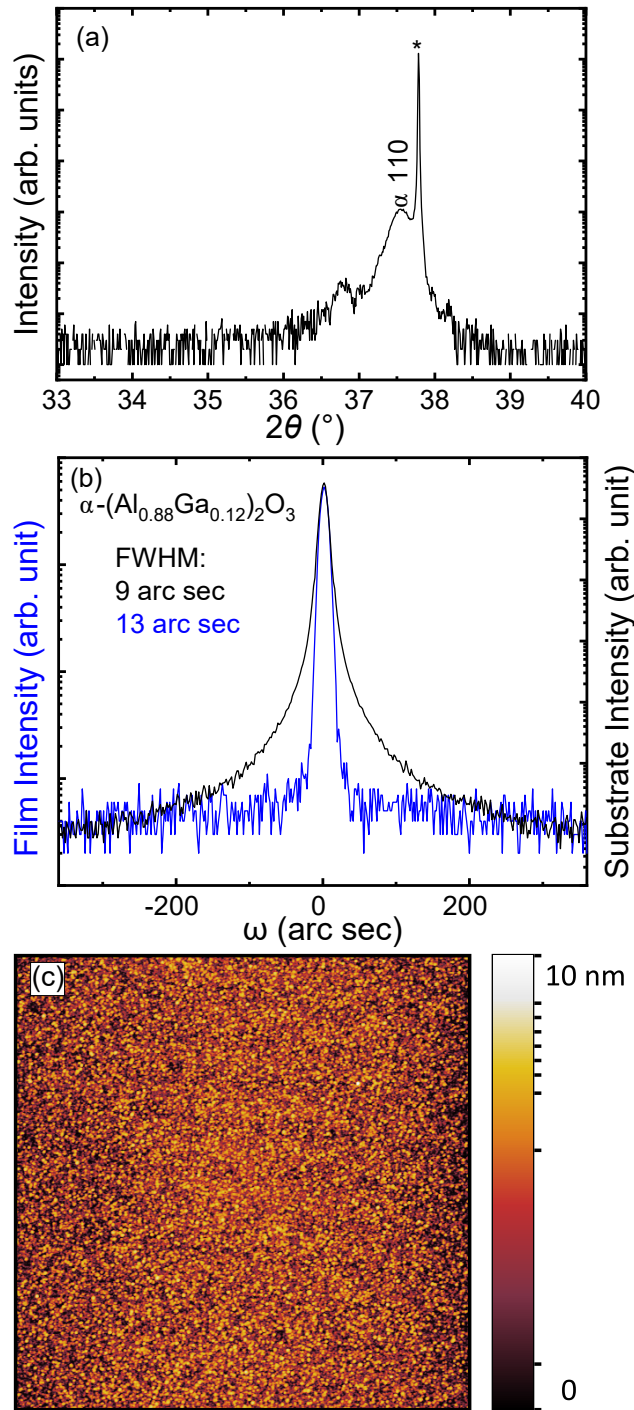


FIG. S14. (a): XRD plot of the  $\alpha$ -(Al<sub>0.88</sub>Ga<sub>0.12</sub>)<sub>2</sub>O<sub>3</sub> film over the range of  $2\theta = 33^\circ - 40^\circ$ . (b): The rocking curve of the film, shown in blue, has a FWHM of 13 arc sec. The rocking curve of the substrate, shown in black, is given as a comparison for the film and has a FWHM of 9 arc sec. (c): AFM shows that the growth surface has a RMS roughness of 0.521 nm on a thickness of 40.8 nm.

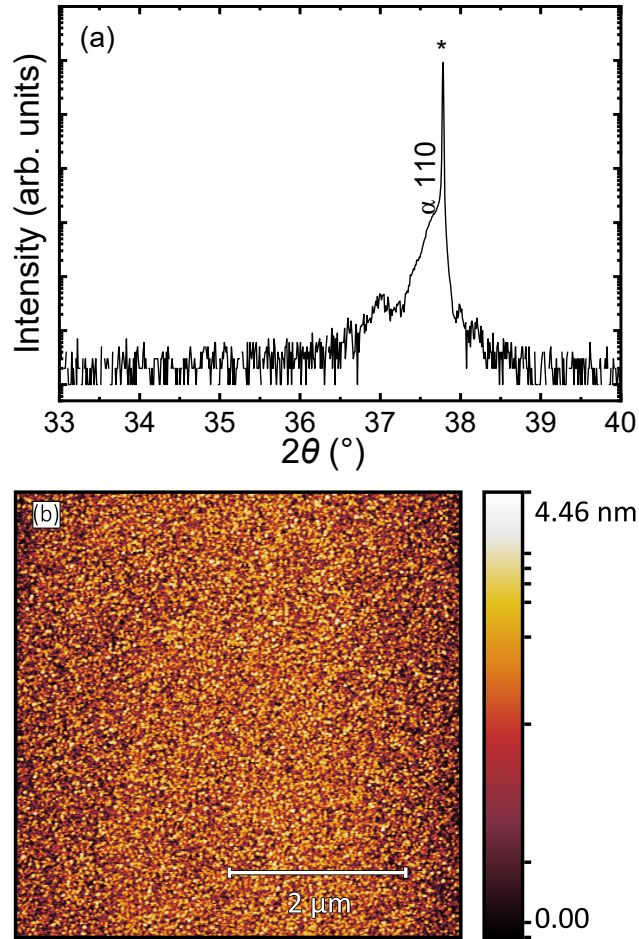


FIG. S15. (a): XRD plot of the  $\alpha$ -(Al<sub>0.95</sub>Ga<sub>0.05</sub>)<sub>2</sub>O<sub>3</sub> over the range of  $2\theta = 33^\circ - 40^\circ$ . (b): The rocking curve of the film, shown in blue, has a FWHM of 11 arc sec. This sample does not have rocking curves since the film peak is close to the substrate peak and leads to mutual interference. (c): AFM shows that the growth surface has a RMS roughness of 0.435 nm on a thickness of 47.8 nm.

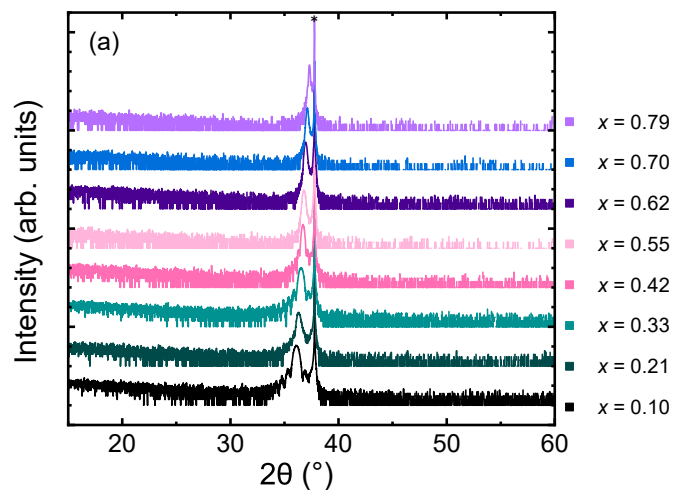


FIG. S16. (a)  $\theta$ - $2\theta$  XRD scans of all of the  $\alpha$ -(Al<sub>x</sub>Ga<sub>1-x</sub>)<sub>2</sub>O<sub>3</sub> films used in the UV-Vis measurements shown in Fig. 6 of the main text. The  $\theta$ - $2\theta$  scans cover the  $2\theta$  range of  $15^{\circ}$  -  $60^{\circ}$ . The plots show that the films are single phase with no additional peaks observed. The composition of each film is identified by the color of the individual plot. The 110 peak for the  $\alpha$ -Al<sub>2</sub>O<sub>3</sub> substrate is marked by a \*.

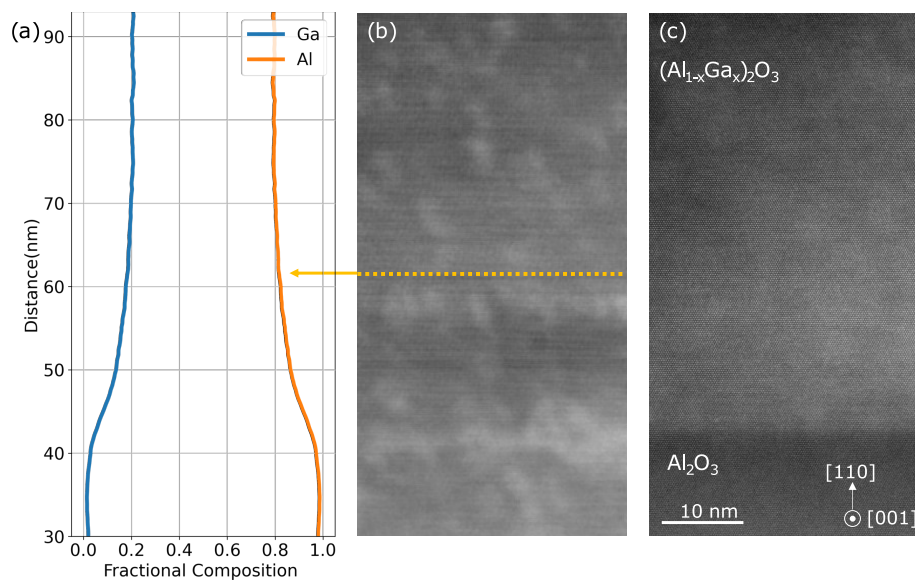


FIG. S17. **(a)** Line profile of fractional composition of aluminum ( $x$ ) and gallium ( $1-x$ ) measured by EDS in STEM across the sapphire to the  $\alpha$ -(Al<sub>0.78</sub>Ga<sub>0.22</sub>)<sub>2</sub>O<sub>3</sub> film interface. The measurement shows a consistent distribution of gallium and aluminum throughout the bulk of the epitaxial film. The sample was tilted 15 degrees during collection of the characteristic EDS x-rays, resulting in a smeared interface. **(b)** HAADF-STEM image of interface region, tilted 15 degrees off-zone. The dotted line represents the data points averaged used to make a single data point in **(a)**. **(c)** HAADF-STEM image of a similar interface region aligned to the zone axis, showing the presence of a clean interface.

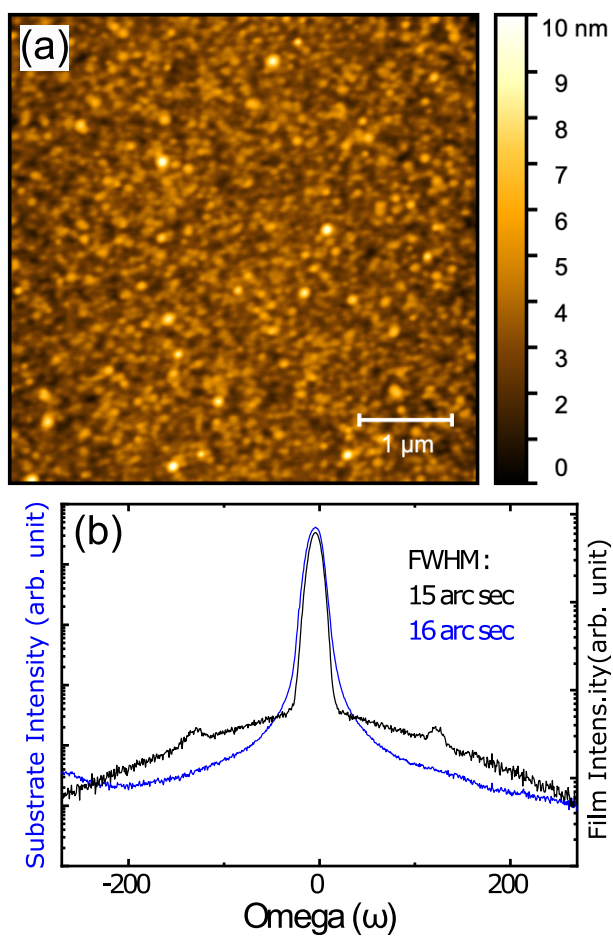


FIG. S18. (a) AFM scan of the  $\alpha$ -(Al<sub>0.78</sub>Ga<sub>0.22</sub>)<sub>2</sub>O<sub>3</sub> film used for STEM measurements. The film is found to have an rms value of 0.89 nm. (b) The rocking curve of the substrate is shown in blue and has a FWHM of 16 arc sec. The rocking curve of the film is shown in black and has a FWHM of 15 arc sec. Both rocking curves are of the 110 peaks. The rocking curves are scaled to have the same maximum intensity to help show the difference in FWHM.